ACS OMEGA

Open Access

http://pubs.acs.org/journal/acsodf

Article

Unveiling Termination Preferences and Screening of Structural Space in Multi-Metal MXenes

Mauricio Mocelim, Henrique A. B. Fonseca, Pedro Ivo R. Moraes, and Juarez L. F. Da Silva*

Cite This: *ACS Omega* 2025, 10, 32310−32325

Read Online

ACCESS | Metrics & More | Article Recommendations | Supporting Information

ABSTRACT: MXenes are promising two-dimensional materials for energy storage, catalysis, and electronics; however, our atomistic understanding of the stability mechanisms that rule the stability and physicochemical properties of multiple-metal MXenes is far from satisfactory. In this study, we investigated the configurational space, structural parameters, energetic stability, and the electronic properties of the MXenes $(M'M'')_{n+1}(X'X'')_nO_2$ family, where M = Mo, Cr, Mn, Nb, V, Ti, Y, and X = C, N, B. We used density functional theory calculations within the Perdew−Burke−Ernzerhof functional including Hubbard corrections for the Cr, Mn, and V *d*-states. We identified a correlation between the magnitude of the occupation of the *M* d_{z^2}-states and the preferential occupation of the O-sites on the MXene surface. Specifically, a reduced occupation of the d_{z^2}-states leads to an energetic preference for the face-centered cubic sites, which is observed in most systems, except for Mo_2CO_2, $CrMoNO_2$, $MoVCO_2$ (Mo side), and $MoNbNO_2$, where a higher occupancy of the d_{z^2}-states promotes a preference for hexagonal close-packed sites. The in-plane configuration, that is, with metals or *X* mixed in the same layer, is more stable for $MnNbCO_2$, $MoNbNO_2$, $NbYBO_2$, Ti_3CNO_2, and Nb_3CNO_2 MXenes, while the out-of-plane configuration, that is, with *M* or *X* separated in different layers, minimized the total energy for $MoVCO_2$, $CrMoNO_2$, and Ti_2NbCNO_2. Furthermore, we found a clear correlation between the work function and surface area and the chemical composition. As expected, the majority of our compositions are metallic, which is advantageous for applications of these materials as electrodes, e.g., in electrochemistry applications.

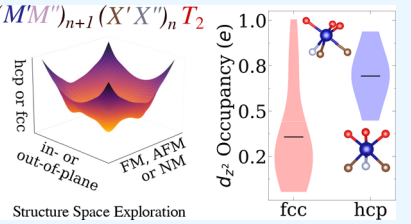

1. INTRODUCTION

MXenes are a promising family of two-dimensional (2D) materials obtained from layered MAX phases ($M_{n+1}AX_n$) by etching the *A* element (group 8−16 element in the periodic table), where *M* is an early transition metal, and *X* are species with smaller atomic radius such as carbon (C), nitrogen (N), or boron (B).[1,2] Therefore, given the potential variations in the selection of the *M*, *A*, and *X* species,[1] a vast array of chemical compositions can be obtained, and hence, it can result in a diverse spectrum of physicochemical properties.[3,4] For example, MXenes have been the subject of extensive research for a variety of applications, such as gas sensors,[5] cathode for sodium-ion batteries,[6] additives for perovskite solar cells,[7] catalysts in the water−gas shift reaction,[8] electrolyzers for hydrogen evolution reaction (HER),[9,10] etc. Thus, the unique versatility and properties of MXenes make them crucial for the advancement of next-generation energy transition technologies.

The MXenes can be represented by the chemical formula $(M'M'')_{n+1}(X'X'')_nT_x$, where *n* ranges from 1 to 4, $M'M''$ are commonly early transition metals elements, while *X* is C, N, B or a combination of them. Finally, *T* is the surface termination with *x* ranging from 0 up to 2. In MXene structures, the metal atoms are stacked in hexagonal closed-packed (hcp) structures, which have a space group of $P63/mmc$.[11] If $M' = M''$, the MXene is called a single-metal compound; otherwise, if $M' \neq M''$, the metal atoms can be separated in different layers or mixed in the same layer, i.e., several structural combinations are possible. The $X'X''$ atoms are located in the octahedral interstitial sites, while the *T* sites can be occupied by O, OH, NH, F, Cl, Br, S, Se, Te or a combination of them located in the hcp or face-centered cubic (fcc) sites.[11] For both *M* and *X* species, the formation of out-of-plane double *M*, *X* (o^M-MXene and o^X-MXene) or in-plane double *M*, *X* (i^M-MXene and i^X-MXene) structures is feasible, i.e., species can be spatially segregated into distinct layers or integrated within the same layer, respectively.

The termination of MXenes, indicated here by *T*, has a strong dependence on the synthesis method. For example, (i) when concentrated hydrogen fluoride (HF) is used, the H^+ oxidizes the *A* element and F^- binds to it, resulting in its removal and F, OH and O terminations; (ii) the use of molten salts has a similar acid−base mechanism but leads to Cl terminations; (iii) when water-free ammonium hydrogen fluoride (NH_4HF_2) is used, the termination is F-rich.[12] However, postsynthesis heating combined with sonication

Received: May 12, 2025
Revised: July 1, 2025
Accepted: July 8, 2025
Published: July 15, 2025

can be used to obtain desirable terminations and single-layer sheets.[2] In addition to these structural possibilities, more recently these materials were predicted to form random solid metal solutions, oxycarbides, or even high-entropy MXenes,[13] i.e., a wide range of possibilities are possible for the structures.

About 40 MXenes have been synthesized experimentally and more than 100 have been predicted by theoretical calculations.[12] Most of the MXenes reported experimentally are carbides; once the layers of nitride are dispersed during treatment with HF. With this discussion, we intend to emphasize that, although MXenes can have diverse compositions and structures, more than 70% of all research studies have focused only on the $Ti_3C_2T_x$ compounds with different terminations due to easy top-down synthesis from stable titanium aluminum carbide (Ti_3AlC_2) precursors.[1] Given the extensive uncharted regions in terms of composition and structural diversity, it is imperative for forthcoming research to extend beyond Ti-based MXenes. Notable examples of successful ventures into nitride exploration include the synthesis of Mo_2NT_x, V_2NT_x, and nitrogen-doped Ti_2CT_x.[14,15]

Theoretical calculations based on density functional theory (DFT) calculations usually assume the fcc sites for T terminations and only out-of-plane MXenes configurations. Several studies have modeled a large number of double-metal MXenes, but only o^M-MXene were considered in the majority of investigations.[16,17] This assumption oversimplifies the exploration of the structure space, e.g., both o^M-MXene and i^M-MXene can be experimentally synthesized.[18] The same problem occurs for carbonitride structures, e.g., only random distribution has been experimentally observed,[19] however, theoretical studies considered only o^X-MXene.[20,21]

In many theoretical studies, especially when considering double-metal MXenes, several assumptions are made, which are not justifiable. In this work, we aim to explore the structure space of MXenes to obtain insights into the atomic structures and their relations to the electronic structure. We selected the following compositions based on recent literature reports as relevant materials for HER, which is a promising application of MXenes: Mo_2CO_2,[22] Cr_2CO_2,[23] $MnNbCO_2$,[17] $MoVCO_2$,[17] $CrMoNO_2$,[17] $MoNbNO_2$,[17] $NbYBO_2$,[17] $Ti_3C_2O_2$,[24,25] Ti_3CNO_2,[20] Nb_3CNO_2,[20] Ti_2NbCNO_2,[21] $V_4C_3O_2$,[26] $Nb_4C_3O_2$,[27,28] $Cr_4C_3O_2$.[29] In our calculations, we considered only O terminations because of its great stability and suitability for HER.[13,17,30,31] Furthermore, by considering only a single termination, it will be possible to perform a deep exploration of the structural configuration space of the MXenes, and hence, a solid contribution to the field of 2D materials.

2. THEORETICAL APPROACH AND COMPUTATIONAL DETAILS

2.1. Total Energy Calculations. Our calculations were based on the spin-polarized DFT[32,33] framework, as implemented in the Vienna Ab initio simulation package (VASP), version 5.4.4.[34] Local or semilocal approximations for the exchange-correlation (XC) energy functional face challenges in describing the long-range van der Waals (vdW) interactions. Thus, to improve the accuracy of our results, we used the semiempirical vdW D3 correction[35] for all calculations, which incorporates an attractive component of the total energy, and adjusts the equilibrium lattice parameters (a_0) closer to the experimental values.[36,37] The semilocal formulation proposed by Perdew−Burke−Ernzerhof (PBE)[38] for the XC energy functional has limitations in providing an accurate description of the localization of the d-states in several MXenes, particularly those compositions that include Cr, Mn, and V, e.g., Cr_2CO_2, $MnNbCO_2$, $MoVCO_2$, $CrMoNO_2$, $V_4C_3O_2$, and $Cr_4C_3O_3$.[4,39,40] In particular, it affects mainly the magnitude of magnetic moments, adsorption site of the T species, and the magnitude of the electronic band gap, however, it yields good equilibrium lattice parameters.[36,41,42]

Based on these observations, we used the following strategy: (i) All MXene structures selected for different compositions were initially optimized using the PBE XC approximation. (ii) All MXenes with Cr, Mn and V in their chemical composition were reoptimized using the PBE + U approximation, which can improve the description of the localization of the d-states, and hence provides an improvement in the description of the physical-chemical properties. Here, we used the rotationally invariant approach[43] with an effective Hubbard parameter (U_{eff}) of 4 eV applied to metals d-states, which yields magnetic properties similar to those obtained by hybrid functionals such as the Heyd−Scuseria−Ernzenhof (HSE).[39]

Electron−ion interactions were described using the full-potential projector augmented wave (PAW) method[44,45] in combination with a set of plane wave bases to represent the Kohn−Sham (KS) states. The MXene structures were modeled using repeated slab geometry with a 2 × 2 unit cell and a vacuum thickness of 15 Å in the z direction, resulting in negligible interactions between the slab and its periodic images. To determine the equilibrium structures, we performed optimizations of the stress tensor components in the xy plane, concurrently with the optimization of forces in all directions.

A plane wave cutoff energy of 868.862 eV was employed, which is twice the largest recommended cutoff energy specified by the selected PAW projectors (Mo, Cr, Mn, Nb, Mo, V, Ti, Y, C, N, B and O) due to the slower convergence of the stress tensor with respect to the number of plane waves. For all optimizations, the equilibrium structure was reached once the atomic forces were smaller than 1×10^{-2} eV Å^{-1} on all atoms using the self-consistency criterion of 1×10^{-6} eV for the total energy. Furthermore, to improve the stability of the self-consistency process, we used a Gaussian smearing parameter of 0.01 eV. For the remaining properties, we used a plane wave cutoff energy of 488.735 eV, that is, 12.5% higher than the largest recommended value.

To obtain an optimum **k**-mesh for each MXene composition, which can yield good results at a lower computational cost, we performed several computational convergence calculations. We considered a maximum error of 1 and 0.75% for cohesive energies (E_{coh}) and a_0, respectively, compared with well-converged results. For example, the equilibrium structure was obtained for one configuration using a unit cell 1 × 1 for each MXene composition as a function of the **k**-meshes, i.e., 4 × 4 × 1, 8 × 8 × 1, 16 × 16 × 1 and 32 × 32 × 1. Thus, we find that a **k**-mesh of 2 × 2 × 1 is enough to produce accurate results for Cr_2CO_2, $MoVCO_2$, $CrMoNO_2$, $MoNbNO_2$, $Ti_3C_2O_2$, Ti_3CNO_2, Nb_3CNO_2, Ti_2NbCNO_2, $V_4C_3O_2$, $Nb_4C_3O_2$, and $Cr_4C_3O_2$ in units 2 × 2, while it is increased for 4 × 4 × 1 **k**-mesh for Mo_2CO_2, $MnNbCO_2$, and $NbYBO_2$. Moreover, for the purpose of calculating the density of states (DOS) and assessing the band structure, the **k**-mesh was expanded to 32 × 32 × 1 and 16 × 16 × 1 for unit cells 1 × 1 and 2 × 2, respectively, to enhance the representation of the electronic states in proximity to the maximum valence band and the minimum conduction band.

https://doi.org/10.1021/acsomega.5c04416
ACS Omega 2025, 10, 32310−32325

2.2. MXenes and Atomic Structure Configurations.

We selected the following compositions of MXenes, which are categorically divided into two groups: experimentally synthesized[23−28,46,47] and theoretically predicted.[17,20,21,29] The first group includes: Mo_2CO_2,[47] Cr_2CO_2,[23] $Ti_3C_2O_2$,[24,25] Ti_3CNO_2,[46] $V_4C_3O_2$,[26] $Nb_4C_3O_2$,[27,28] and Ti_2NbCNO_2,[21,48] while the second group includes: $MnNbCO_2$,[17] $MoVCO_2$,[17] $CrMoNO_2$,[17] $MoNbNO_2$,[17] $NbYBO_2$,[17] Nb_3CNO_2,[20] and $Cr_4C_3O_2$.[29] MXenes with Mo and V have been synthesized, but only for a larger number of layers, e.g., MoV_3C3T_x.[49] For $Ti_{2-y}Nb_yCT_x$, there are reports of synthesis with various compositions with unlimited solubility and random distribution of metals.[48]

Figure 1 shows a schematic representation for MXenes with *ABC* stacking (*M* and *X* layers). This stacking was considered because the MAX phases, which are precursors of MXenes, are generally more stable for *ABC* stacking.[50] For the considered MXenes compositions, to the best of our knowledge, there are no experimental reports of preference for *AB* stacking.[51] The MXene structures can differ in the preference of the surface termination site and in the number of *M* layers. Furthermore, more than one species can be found in the metal and *X* layers, and hence larger unit cells are required to model these systems. In this work, we used a 2 × 2 unit cell, which yields additional configurations for the structure space. Thus, the selected MXenes are single or double-metals with the formula $(M'M'')_{n+1}(X'X'')_nO_2$, where M' and M'' represent metal species, while X' or X'' is either C, N or B. The O species are located within the fcc or hcp sites. Moreover, a number of the selected MXenes exhibit magnetic properties, necessitating the consideration of nonmagnetic (NM), ferromagnetic (FM), ferrimagnetic (FIM) and antiferromagnetic (AFM) configurations, which increases the number of calculations substantially.

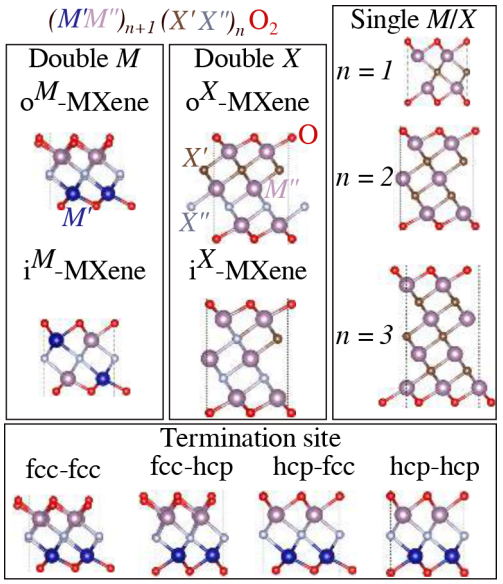

Figure 1. Schematic representation of the selected MXenes structures, including *M* and *X* species forming in-plane and out-of-plane structures, fcc and hcp *T* surface terminations, and MXenes with different numbers of layers.

Figure 2 shows a schematic representation of the exploration of the configuration space to obtain the lowest energy configurations for the selected MXenes. Based on this diagram, it yields about 240 stress tensor calculations, which can be explained as follows: (i) Initially, we considered the initial configurations of o^M-MXenes, i^M-MXenes, o^X-MXenes, i^X-MXenes, FM, and AFM. We also considered fcc and hcp sites for oxygen termination; (ii) We further explored only the most promising region, for example, for Nb_3CNO_2, after initial exploration, the lowest energy region was fcc-fcc-i^M-MXene, then we calculated several other configurations of i^M-MXene to obtain the lowest energy structure. All systems with a total magnetic moment of 0.1 μ_B/atom were classified as FM or FIM; (iii) For systems containing Cr, Mn or V, we further explored the structure space using PBE + *U*, that is, we considered different structures from PBE calculations within a range of 100 meV.

3. RESULTS AND DISCUSSION

The most significant trends and results derived from this study are summarized and analyzed below. We begin our discussion

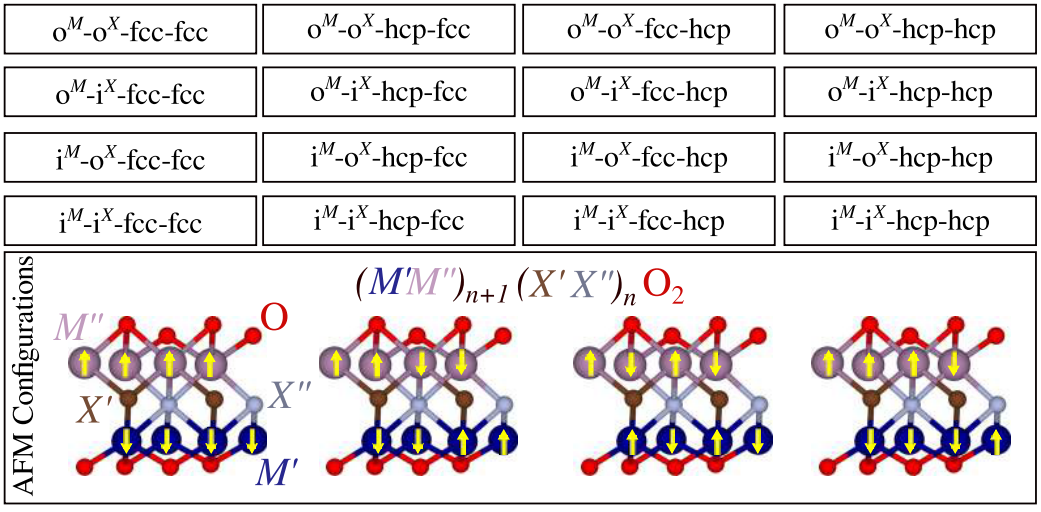

Figure 2. Schematic representation of structure possibilities for the out-of-plane and in-plane MXenes, represented by the letters o- and i-, respectively. The possible oxygen sites are labeled as fcc or hcp. The electronic AFM, FM, FIM, and NM configurations were considered but are not shown here.

https://doi.org/10.1021/acsomega.5c04416
ACS Omega 2025, 10, 32310−32325

with all results from the structural space exploration, namely the PBE calculations. Then, we discuss the differences between PBE + vdW and PBE + vdW + U for the selected systems. Finally, we focus on the lowest energy structures, which include several physical-chemical properties. We applied ligand field theory (LFT) to the lowest-energy structures to explain termination sites. We also analyzed the covalent, ionic, and metallic character of chemical bonds in MXenes. Finally, we explore the relationship between bond character and the band gap of the systems. In the last section, we discuss potential applications of MXenes based on the knowledge obtained throughout this paper.

3.1. Screening of the Structural Configurational Space via PBE Calculations. *3.1.1. Relative Energies.* Figure 3 summarizes the relative total energy (ΔE_{tot}) for all optimized configurations, where $\Delta E_{tot} = E^{i}_{tot} - E^{lowest}_{tot}$. E^{i}_{tot} is the total energy of the configuration i and E^{lowest}_{tot} is the lowest total energy configuration. We found that most of the optimized structures are within ΔE_{tot} of 301.785 meV/atom. The exception is $MnNbCO_2$, where the highest energy is at 631.998 meV/atom. Furthermore, there are many configurations within the relative total energy precision limit, i.e., smaller than 5 meV/atom. For example, several FIM, AFM, and NM configurations obtained for Cr_2CO_2, $CrMoNO_2$, and $Cr_4C_3O_2$ are degenerate.

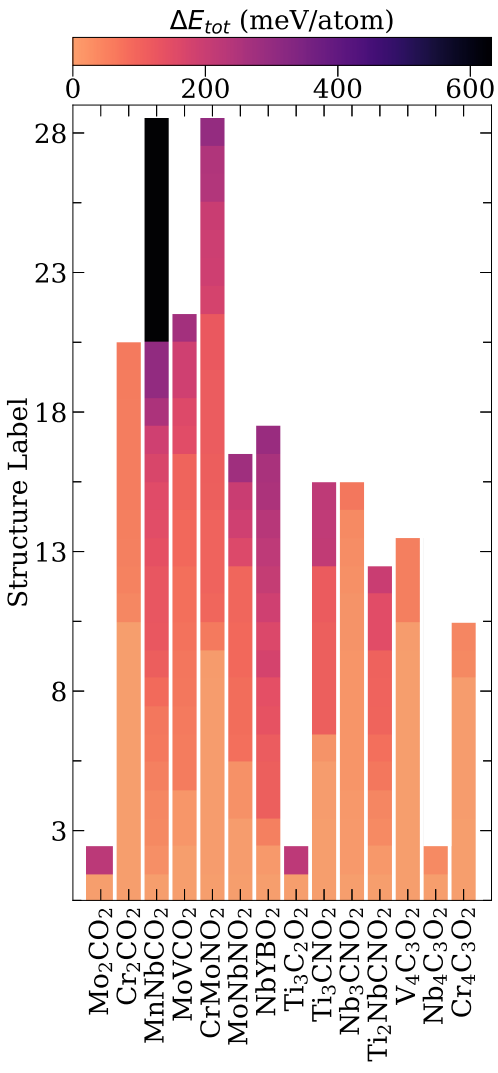

Figure 3. Heat map of the PBE ΔE_{tot} results for all optimized MXene configurations. The structure labels on the y-axis are provided solely for visual representation, where each point on the y-axis corresponds to a specific configuration. The energies and configurations of all calculations, including in- and out-of-plane, hcp, fcc, and magnetic configurations, are available in the electronic Supporting Information file. Single metal NM systems have few possibilities, while the number of structural/magnetic configurations increase for double metal magnetic systems, specially due to assessment of AFM possibilities.

3.1.2. Termination Site. For most systems, the O species have an energetic preference for the fcc sites, whereas the hcp sites are obtained for systems composed of Mo atoms. The behavior discussed previously does not occur in $MoNbNO_2$ because these i^M-MXene have an equal number of both metals in each layer. Systems with Nb atoms prefer the fcc sites in most cases, except for $MoNbNO_2$ due to the presence of Mo, as discussed before. We will return to this discussion of the fcc or hcp preference in Section 3.5, where we discuss electronic structure.

3.1.3. In- and Out-of-Plane. All carbonitrides have a preference for the i^X-MXene, except for Ti_2NbCNO_2. These results can guide other theoretical works, i.e., o^X-MXene should not be the first choice of structure. For double-metal MXenes, our results indicate that only structure exploration can lead to the lowest energy structure, i.e., half of our MXenes prefer i^M-MXene structures while the other half prefers o^M-MXene structures.

3.2. Investigation of the Role of the Hubbard U Correction. As shown in Table 1, the addition of Hubbard correction U (PBE + U) in MXene systems containing Cr, Mn, and V induces significant changes in both their structural and electronic/magnetic properties, which is consistent with previous results.[4,39] For example, in general, the addition of U results in a modest increase in the thicknesses a_0 and MXene thicknesses (d_z) across all selected compounds. This behavior aligns with a decrease in the delocalization of d-states, which consequently weakens the covalent bonding and leads to expanded interatomic distances. As expected from previous studies,[4,39] PBE + U tends to enhance the magnitude of local magnetic moments (m_{loc}) and, in numerous instances, modifies the total magnetic moment (m_{tot}) of the unit cell. For example, MXenes characterized as NM or exhibiting weak magnetism under PBE frequently become magnetically ordered under the PBE + U approximation, exhibiting FM or AFM configurations. Furthermore, while several systems remain metallic after incorporation of U, others undergo a bandgap (E_g) opening or widening. For certain systems, PBE + U predicts a divergent lowest-energy configuration relative to PBE, underscoring the necessity of accounting for localization effects in structural optimizations.

The magnitude of the effects induced by the addition of the Hubbard U correction is different for each system. For example, Cr_2CO_2 shows a substantial response to the addition of U: (i) The favored O termination changes from hcp (PBE) to fcc (PBE + U), with a significant increase in a_0 from 2.68 to 3.01 Å; (ii) PBE predicts a metallic solution, while PBE + U yields a moderate E_g of (0.36 eV) along with the development of considerable local magnetic moments on the Cr atoms, which are arranged AFM. With respect to $MnNbCO_2$, the structural configuration remains unchanged (i-fcc-fcc) with PBE + U, although a_0 expands from 3.01 to 3.14 Å. The metallic nature is retained; nevertheless, the magnetic properties are considerably modified: the total magnetic moment

https://doi.org/10.1021/acsomega.5c04416
ACS Omega 2025, 10, 32310−32325

Table 1. Comparison between the PBE and PBE + U for MXenes Compositions with Cr, Mn or V[a]

system	final conf.	functional	a_0	d_z	E_g	m_{tot}	$m_{loc}^{M'}$	$m_{loc}^{M''}$
Cr_2CO_2	hcp	PBE	2.68	4.85	metal			
	fcc	PBE + U	3.01	4.93	0.36	0.00	2.41	
$MnNbCO_2$	i-fcc-fcc	PBE	3.01	4.55	metal	8.10	2.19	0.11
		PBE + U	3.14	4.61	metal	16.48	4.26	0.06
$MoVCO_2$	o-hcp-fcc	PBE	2.89	4.80	metal	3.54	0.06	0.85
		PBE + U	2.92	4.81	metal	4.03	0.04	1.18
$CrMoNO_2$	o-fcc-hcp	PBE	2.87	4.85	0.56	10.84	2.58	0.09
	o-hcp-hcp	PBE + U	2.89	4.91	0.87	0.00	2.62	0.03
$V_4C_3O_2$	fcc	PBE	2.85	9.23	metal			
		PBE + U	2.96	9.35	metal	0.00	0.80	
$Cr_4C_3O_2$	hcp	PBE	2.77	9.50	metal	0.00	0.28	
	fcc	PBE + U	2.94	9.38	metal	32.46	2.35	

[a]In this table, we show only the lowest energy structure for each functional. We show the average of a_0 and b_0 and d_z, in Å. The E_g is given in eV. The m_{tot} and m_{loc} are the total and modulus of metal local magnetic moments in units of (μ_B) and (μ_B/atom), respectively.

nearly doubles and the local Mn moment increases from 2.19 to 4.26 μ_B/atom, indicating a substantial enhancement of the magnetic ordering under PBE + U.

For compound $MoVCO_2$, the structural configuration of o-hcp-fcc is consistently retained between PBE and PBE + U, the material that maintains its metallic nature. Only marginal increases are observed in both a_0 and d_z, and the alterations in magnetic properties are comparatively moderate: a minor increase in total magnetic moment and an enhancement of the local magnetic moment in V from 0.85 to 1.18 μ_B/atom. In contrast, for $CrMoNO_2$, there is a structural transition from o-fcc-hcp (PBE) to o-hcp-hcp (PBE + U), accompanied by a slight increase in a_0. For $V_4C_3O_2$, the T site is retained for both approximations and we observed a notable increase in a_0, that is, a difference of 0.17 Å between PBE and PBE + U. A similar increase occur for d_z, however the material retains its metallic nature for both approximations. Furthermore, the lowest energy structure changes from NM to AFM with a m_{loc} of 0.80 μ_B/atom.

We found significant changes for $Cr_4C_3O_2$: the structural configuration changes from hcp as determined by PBE to fcc as determined by PBE + U, which is accompanied by a substantial increase in the lattice parameter. PBE + U indicates a significant alteration in magnetic properties, in which the total magnetic moment escalates from zero to 32.46 μ_B, and the local Cr moments become markedly larger, suggesting intensified ferromagnetic ordering.

For Cr_2CO_2, Bera and Kumar found a metallic FM structure in their work,[4] however, they considered 2 × 1 supercells, and we should highlight that, as energy differences are in the range of meV/atom, different computational parameters play an important role, e.g., the **k**-mesh, supercell size, and initial magnetic configuration. Another evidence of the complexity of Cr_2CO_2 is the fact that Tan et al.[39] found a hcp-FM lowest energy structure, but the energy differences in their work were also within a range of meV/atom. For $V_4C_3O_2$, our a_0 from PBE + U matches the experimental results available.[52] For the other systems, we found no studies in the literature for comparison.

3.3. Structure Features of the Lowest Energy Configurations. Figure 4 shows the lowest energy structure for each composition from our PBE and PBE + U calculations. In the following, we summarize the most important results. Our calculations show that the fcc O-terminations minimize energy for most cases, namely Cr_2CO_2, $MnNbCO_2$, $MoVCO_2$ (V side), $NbYBO_2$, $Ti_3C_2O_2$, Ti_3CNO_2, Nb_3CNO_2, Ti_2NbCNO_2, $V_4C_3O_2$, $Nb_4C_3O_2$, and $Cr_4C_3O_2$. The remaining systems prefer hcp O-terminations, namely, Mo_2CO_2, $MoVCO_2$ (Mo side), $CrMoNO_2$, and $MoNbNO_2$.

The i^M-MXenes are more stable for $MnNbCO_2$, $NbYBO_2$, and $MoNbCO_2$ while o^M-MXene minimizes the energy in $CrMoNO_2$, Ti_2NbCNO_2, and $MoVCO_2$. Carbonitrides are more stable in the i^X-MXene configuration, except Ti_2NbCNO_2. Our results are consistent with the literature for the systems Mo_2CO_2 and $V_4C_3O_2$.[52,53] For Ti_3CNO_2, Nb_3CNO_2, and Ti_2NbCNO_2 the literature has only considered o^X-MXenes,[20,21] but our calculations show that i^X-MXenes yield the lowest energy.

The systems $MoNbNO_2$ and $NbYBO_2$ were previously investigated in the literature; however, only fcc-fcc-o^M-MXene structures were considered, as exemplified in the machine learning work by Abraham et al.[17] Our calculations demonstrate that for both systems, hcp-hcp-i^M-MXene structures represent the lowest energy configurations. Interestingly, in the 2 × 2 cell $NbYBO_2$ structure, three of the B atoms are aligned in the lowest energy structure; see Figure 4. The $NbYBO_2$ MXene (MBene) has not yet been synthesized. Previous literature reports for other MBenes indicate that these materials can have hexagonal or orthorhombic structures.[54,55] Our results indicate that this subclass of materials should be further explored theoretically and experimentally. To date, we do not have experimental work to compare these results for $NbYBO_2$. A similar distortion of X sites was also observed for Cr_2CO_2. With regard to electronic structure, the lowest-energy structure of most systems is NM, which is expected for oxygen-terminated MXenes. The systems $MnNbCO_2$ and $MoVCO_2$, and $Cr_4C_3O_2$ are FIM. For Cr_2CO_2, $CrMoNO_2$ and $V_4C_3O_2$ the lowest energy structure was calculated as AFM.

3.4. Lattice Parameters, Cohesive Energies, and Magnetic Trends in MXenes. In Table 2, we present the structural, energetic, electronic, and magnetic properties of the lowest-energy configurations calculated with the PBE and PBE + U. For the equilibrium lattice parameters, we report only the average of a_0 and b_0 because the differences between these constants are negligible (smaller than 0.083 Å for Cr_2CO_2), reinforcing the near hexagonal symmetry of the structures. Individual values of a_0 and b_0 are available in the electronic Supporting Information file. Our lattice constants agree excellently with the values in the literature for Mo_2CO_2, $Ti_3C_2O_2$, Ti_2NbCNO_2, and $V_4C_3O_2$. For example, for

https://doi.org/10.1021/acsomega.5c04416
ACS Omega 2025, 10, 32310−32325

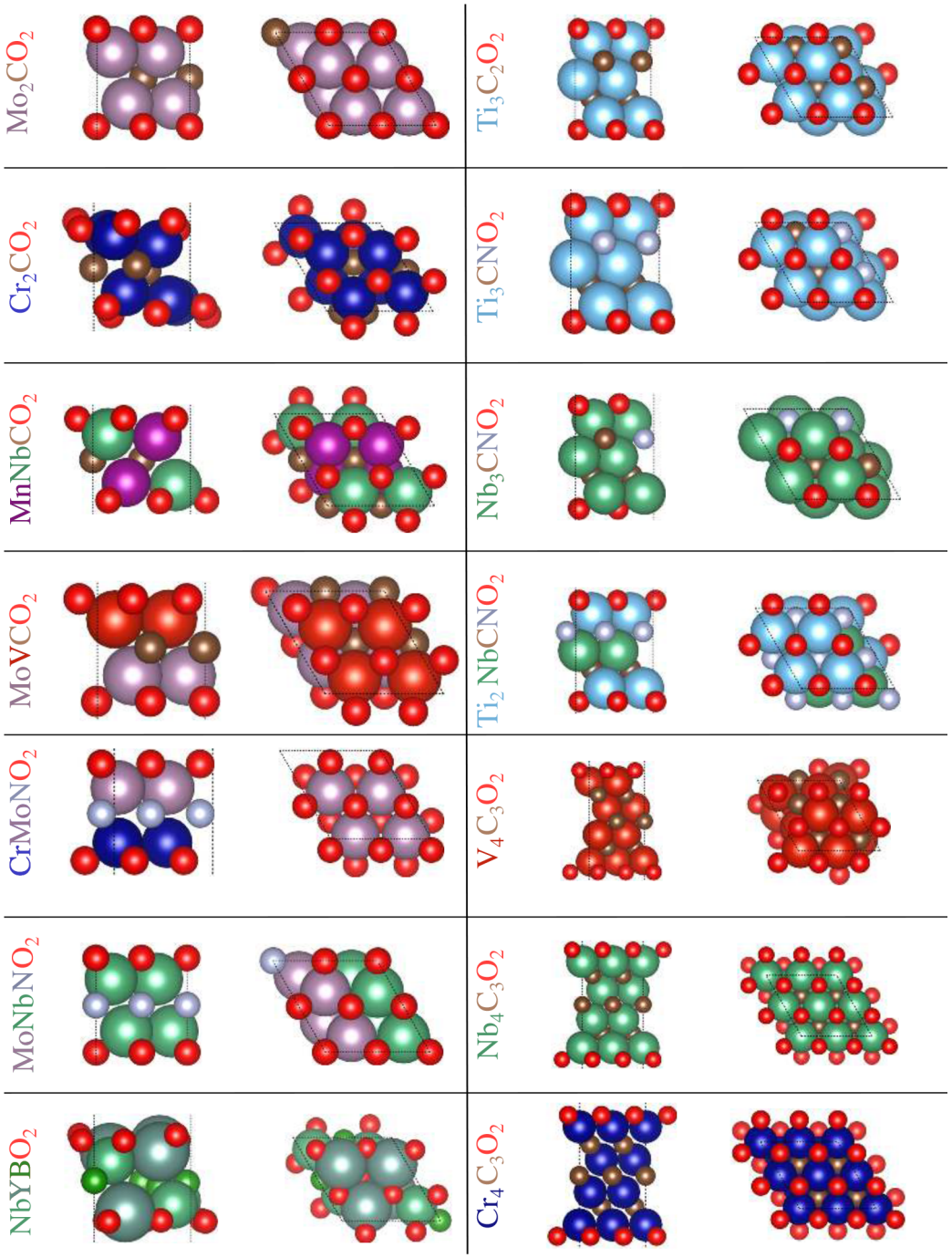

Figure 4. Side (left) and top (right) views of the lowest energy structures for all MXene compositions.

Ti_3CNO_2, Nb_3CNO_2, and Ti_2NbCNO_2, the reported experimental or theoretical values of 3.00, 3.14, and 3.04 Å, respectively,[20,21] are consistent with our findings. However, comparisons must be made cautiously, given that the literature values are for o^X-MXenes, while our work is focused on i^X-MXene phases, which involve different stacking sequences of nonmetal (X) layers.

The cohesive energy (E_{coh}) is a direct measure of the energetic stability of a material, reflecting the strength of the chemical bonding network. It was calculated as follows:

$$E_{coh} = \frac{E^i_{tot} - \sum_{n=1}^{N_{atoms}} E^{atoms,n}_{tot}}{N_{atoms}} \quad (1)$$

where E^i_{tot} is the total energy of MXene and $E^{atoms,\,n}_{tot}$ are the isolated atomic energies. As expected from chemical bonding principles, thicker MXenes (those with more atomic layers or larger d_z) tend to exhibit more negative E_{coh}, indicating greater thermodynamic stability. This can be rationalized by considering that thicker structures benefit from enhanced metallic bonding interactions, effectively reducing the energy per atom. For example, Ti_2NbCNO_2 presents the most negative E_{coh} among double metal systems (−8.08 eV/atom), suggesting that it would be particularly resistant to decomposition, while thinner structures such as Cr_2CO_2 and $CrMoNO_2$ are energetically less stable. This trend is crucial for practical applications; for example, materials with lower

https://doi.org/10.1021/acsomega.5c04416
ACS Omega 2025, 10, 32310−32325

Table 2. Lowest Energy MXenes, Average of a_0 and b_0, and d_z, in Å[a]

system	a_0	d_z	E_{coh}	E_g	m_{tot}	$m_{loc}^{M'}$	$m_{loc}^{M''}$	Φ
Mo_2CO_2	2.86 (2.88[53])	5.18	−6.61	metal (metal[22,56])	NM	NM		7.34 (6.75[56])
Cr_2CO_2	3.01	4.93	−4.20	0.36	0.00	2.41		6.11
$MnNbCO_2$	3.14	4.61	−5.36	metal	16.48	4.26	0.06	5.64
$MoVCO_2$	2.92	4.81	−5.44	metal	4.03	0.04	1.18	7.18/6.40
$CrMoNO_2$	2.89	4.91	−4.54	0.87	0.00	2.62	0.03	7.42/6.64
$MoNbNO_2$	2.89	5.21	−6.71	metal	NM	NM	NM	6.81
$NbYBO_2$	3.40	5.21	−6.71	0.08	NM	NM	NM	3.75/4.12
$Ti_3C_2O_2$	3.02 (3.03[57])	6.95	−7.36	metal (metal[57])	NM	NM		6.02 (6.18[58])
Ti_3CNO_2	3.00	6.90	−7.29	metal	NM	NM		5.88
Nb_3CNO_2	3.11	7.33	−7.44	metal	NM	NM		5.56
Ti_2NbCNO_2	3.04 3.04[21]	6.95	−8.07	metal	NM	NM	NM	5.66/5.58
$V_4C_3O_2$	2.96 (2.95[52])	9.35	−6.03	metal	0.00	0.80		6.30
$Nb_4C_3O_2$	3.14	9.79	−7.80	metal	NM	NM		5.55 (6.39[59])
$Cr_4C_3O_2$	2.94	9.38	−4.21	metal	32.46	2.35		7.07

[a]E_{coh} in eV/atom, E_g in eV, and work function (Φ), given in eV. m_{tot} is the total magnetic moments in the 2 × 2 supercells, while m_{loc} are the metals local magnetic moments normalized by the number of atoms; in units of (μ_B) and (μ_B/atom), respectively. For non-symmetric MXenes, we show both values of the Φ according to the metal order, e.g., for $(M'M'')_{n+1}(X'X'')_nO_2$, the first (second) value is for the side with M' (M''). Results from literature works are shown in parentheses.

Table 3. Nominal Charge of Cations (Q_n) and Average DDEC6 Charges (Q_{av}) of the Lowest Energy MXenes, Given in e/Atom[a]

system	$Q_n^{M'}$	$Q_n^{M''}$	$M'd^{occ}$	$M''d^{occ}$	structure	$Q_{av}^{M'}$	$Q_{av}^{M''}$	$Q_{av}^{X'}$	$Q_{av}^{X''}$	Q_{av}^{O}
Mo_2CO_2	4.0		2		hcp	1.15		−1.24		−0.52
Cr_2CO_2	4.0		2		fcc	1.55		−1.33		−0.88
$MnNbCO_2$	3.0	4.0	4	0	fcc-fcc	1.03	2.19	−1.58		−0.82
$MoVCO_2$	4.0	4.0	2	1	hcp-fcc	1.35	1.76	−1.66		−0.73
$CrMoNO_2$	3.0	4.0	3	2	hcp-hcp	1.47	1.29		−1.30	−0.73
$MoNbNO_2$	4.0	3.0	2	2	hcp-hcp	1.07	1.26		−1.16	−0.59
$NbYBO_2$	4.0	3.0	1	0	fcc-fcc	1.55	1.50	−1.29		−0.88
$Ti_3C_2O_2$	4.0		0		fcc	1.84		−1.82		−0.94
Ti_3CNO_2	3.7		1		fcc	1.83		−1.96	−1.65	−0.95
Nb_3CNO_2	3.7		4[b]		fcc-fcc	1.50		−1.70	−1.27	−0.77
Ti_2NbCNO_2	3.0	5.0	1	0	fcc-fcc	1.86	1.46	−1.73	−1.51	−0.97
$V_4C_3O_2$	4.0		1		fcc	1.72		−1.70		−0.89
$Nb_4C_3O_2$	4.0		1		fcc	1.50		−1.49		−0.77
$Cr_4C_3O_2$	4.0		2		fcc	1.47		−1.41		−0.82

[a]We considered the general formula $(M'M'')_{n+1}(X'X'')_nO_2$. For the nominal charge of oxygen, carbon, nitrogen, and boron, we considered −2, −4, −3, and −3, respectively. The d-states occupancy is represented by d^{occ} and is the number of non-bonding electrons per atom, following the electron counting rule. The electronic configuration of the free atoms is available in the SI. We used the following terminology in this table: fcc-hcp for $(M'M'')_{n+1}(X'X'')_nO_2$ means that the oxygen in M' (M'') side prefers fcc (hcp) site. [b]The d^{occ} for Nb_3CNO_2 is the sum of nonbonding d electrons for the three Nb atoms.

stability might be more suitable for defect engineering or surface modifications,[60] whereas more stable MXenes are promising candidates for robust coatings and electronic devices.

From an electronic perspective, most MXenes exhibit metallic behavior, as indicated by their zero E_g. This is consistent with the delocalized nature of d-states in transition metals, which dominate the DOS at the Fermi level. The exception is $CrMoNO_2$, which exhibits a moderate E_g of 0.87 eV, suggesting a potential for semiconducting applications where a small but nonzero E_g is advantageous. Furthermore, Cr_2CO_2 shows a small E_g (0.36 eV), qualitatively aligning with previous findings using hybrid functionals.[39] For the three semiconductor systems, we observed the smaller E_g for $NbYBO_2$.

With respect to magnetism properties, electronic filling and hybridization between metal d- and oxygen p-states play a decisive role. As a general rule, surface functionalization (e.g., with O, OH, or F groups) quenches unpaired electrons and magnetism by saturating dangling bonds and leading to filled or empty d-bands.[4] This is observed in most systems here, which are nonmagnetic. However, some systems exhibit magnetic order: Cr_2CO_2, $CrMoNO_2$, and $V_4C_3O_2$ adopt AFM solutions, reflecting incomplete spin compensation between neighboring transition-metal atoms. In particular, Cr_2CO_2 is intriguing because DFT-PBE predicts a metallic NM

https://doi.org/10.1021/acsomega.5c04416
ACS Omega 2025, 10, 32310−32325

phase,[61,62] while DFT-HSE calculations favor a semiconductor ferromagnetic (FM) ground state with significant magnetic moments.[39] In our PBE + U calculations, although the AFM configuration is energetically favored, the local magnetic moments (2.41 μ_B/atom) and E_g agree well with the HSE values, indicating the robustness of the local moment formation.

Moreover, several double-metal MXenes ($MnNbCO_2$, $MoVCO_2$, $CrMoNO_2$) show significant total magnetic moments (e.g., 16.475 μ_B for $MnNbCO_2$), primarily localized in one of the transition metals, emphasize the possibility of tailoring magnetic properties by selective metal mixing. This magnetism is particularly promising for spintronics applications.

3.5. Structure Stability Analyses via Ligand Field Theory. *3.5.1. Nominal Charges.* To obtain insights into the relationship of the atomic and electronic structure, we applied LFT. According to the LFT, in fcc-terminated MXenes, the octahedral field around the metal splits the d-states into two energy levels, namely, a lower energy t_{2g}-state (d_{xy}, d_{yz}, and d_{xz}) and an antibonding e_g^*-state (d_{z^2} and $d_{x^2-y^2}$).[4] The importance of d-states splitting has only been realized recently in the literature, in the systematic theoretical work of Bera.[4] Other experimental works have discussed the d-states splitting, but only octahedral environments were considered.[63,64] Therefore, we aim to extend the LFT to our MXenes compositions, which include a large variety of structural possibilities, as discussed in the methodology section.

Table 3 shows the nominal charge of metals and the number of nonbonding d electrons. Our MXenes follow the expected trends; that is, d^2 MXenes prefer trigonal prismatic environments, and any other occupancy of d leads to octahedral environments. However, for Cr_2CO_2, $CrMoNO_2$ (Cr side) and $Cr_4C_3O_2$, our calculations and LFT predictions are different, probably caused by the Hubbard corrections, which change the number of nonbonding states. This analysis is easier for single-metal MXenes than for double-metal MXenes; for example, o^M-MXene $MoVCO_2$ prefers a trigonal (octahedral) environment for the Mo (V) sides. In terms of LFT, this can be rationalized if both metals have equal charges, leading to d^2 and d^1 configurations. It is important to note that this choice is not unique, which makes the analysis difficult.

3.5.2. Effective Charge Analysis. To proceed further, we calculated electrostatic and chemical (DDEC6) charges, which are shown in Table 3. The DDEC6 analysis, as with other charge analyses, considers the flexibility in determining how to allocate the overall electron distribution among the atoms. In Bader charges, for example, because the electron density is continuous, the minimum in the electronic density between atoms is the point that separates the electronic density of one atom from another.[65] The DDEC6 analysis has a different approach: (*i*) one electron distribution is assigned for each atom; and (*ii*) core electrons are assigned to the host atom.[66] The main advantage of this approach is that reference ions are used, which makes the DDEC6 applicable to various materials; e.g., an oxygen anion in any material should resemble the reference ions O^{2-}.

All metals are positively charged with values ranging from 1.03 to 2.19 e/atom. As expected for carbonitrides and borides, most of the negative charge is in the X elements, with values ranging from −1.96 to −1.16 e/atom. The oxygen terminations are negatively charged, that is, values ranging from −0.97 to −0.52 e/atom, which is due to the smaller coordination of the termination groups in MXenes. Furthermore, we observed that O has more negative charges at the fcc sites, which is explained by the coordination environment, that is, in the fcc sites, O is above the hollow site of the metals. However, for the hcp site, O lies above the electronegative X site, which causes a more homogeneous charge displacement.

For all systems, there is no quantitative match between nominal and DDEC6 charges, which is expected due to charge partitioning. For single-metal MXenes, there is qualitative agreement. For $MnNbCO_2$, the calculated charge on Mn and Nb are 1.03 and 2.19 e/atom, respectively, so it is justifiable to place more positive charges on Nb, in accordance with our nominal charges. The same behavior was observed for $NbYBO_2$. However, for systems $MoVCO_2$, $CrMoNO_2$, $MoNbNO_2$, and Ti_2NbCNO_2, there is neither quantitative nor qualitative agreement between the nominal charges and the calculated DDEC6 charges. Thus, the LFT can be easily applied to single-metal MXenes to predict the lowest energy structures; however, for double-metal MXenes, it is difficult to correlate the lowest energy structure only from nominal or calculated charges on metals.

3.5.3. Occupation of the d-States. To further investigate the role of the d_{z^2}-states at the surface O-termination sites, we calculated the integrated projected DOS, that is, we integrated the d_{z^2}-states as

$$d_{z^2}\text{Occupancy} = \int_{-80\text{eV}}^{E_{\text{Fermi}}} \text{LDOS}(E)\text{d}E \tag{2}$$

where E_{Fermi} is the Fermi energy and dE represents the integration variable, that is, the energy of the states. For semiconductor systems, we used the VBM instead of E_{Fermi}. LDOS is the local density of states for the d_{z^2}-states. We used −80 eV, as it corresponded to the lowest energy state observed in our calculations.

Our results in Figure 5 show that systems with hcp preference have a larger d_{z^2}-states occupancies, even for

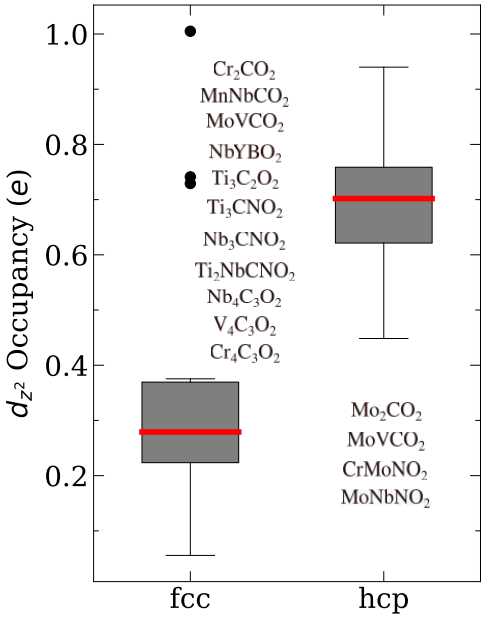

Figure 5. Analysis of d_{z^2}-states occupancies calculated via integration of local density of states until the Fermi level for metallic systems or valence band maximum for semiconductor systems. The red lines represent the medians.

https://doi.org/10.1021/acsomega.5c04416
ACS Omega 2025, 10, 32310−32325

double-metal MXenes. These results extend the LFT to a larger class of materials, i.e., single- and double-metal MXenes, including in- and out-of-plane MXenes. The outliers in Figure 5 are Cr_2CO_2, $MnNbCO_2$, and $Cr_4C_3O_2$; these outliers imply that the application of LFT to systems with Hubbard corrections is more complicated. Furthermore, we should emphasize that this analysis is qualitative, since the integration of the LDOS using plane waves as a basis set for DFT calculations does not account for interstitial density due to the projection scheme. The complete results of electronic states occupancies are available in the SI.

3.6. Work Function versus Surface Composition. We calculated the work function (Φ) to understand its variation as a function of the composition of MXene. The Φ is orientation dependent and represents the minimum energy required for an electron to escape from a solid:[67]

$$\Phi = V_{es}(\mathbf{r}_{vac}) - E_{Fermi} \quad (3)$$

where $V_{es}(\mathbf{r}_{vac})$ is the electrostatic potential in the middle of the vacuum region of the slab, and E_{Fermi} is the Fermi energy. However, for semiconductor systems, we used the valence band maximum (VBM). Table 2 shows the values Φ for all the lowest energy structures, while Figure 6 shows the correlation of Φ and surface area.

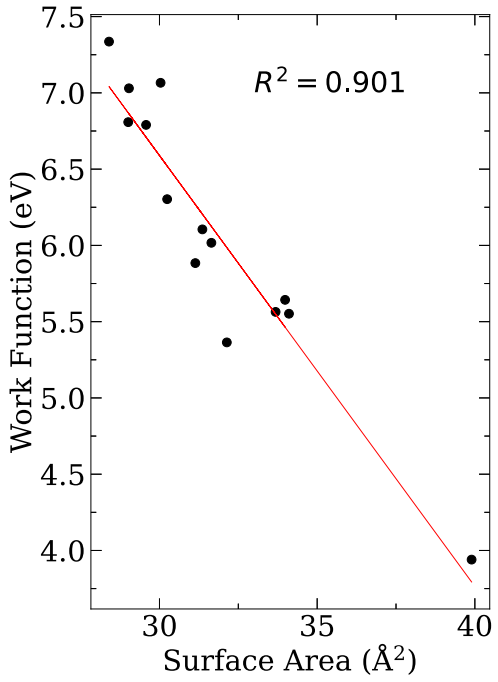

Figure 6. Correlation of work function and surface area. For nonsymmetric MXenes, we considered the average work function for the correlation.

Our Φ values (Table 2 vary considerably among the MXenes. Systems containing Mo, Cr, and V generally have high work functions (Φ > 6.0 eV), associated with strong metallic bonding and dense electronic clouds, while those containing systems Nb or Y exhibit lower values ($\Phi \sim$ 3.75 eV) for $NbYBO_2$). In particular, asymmetric MXenes such as $MoVCO_2$ and $CrMoNO_2$ exhibit two distinct Φ depending on the termination side, which can be used to design devices with tailored directional electron emission or Schottky barriers.

We found that Φ increases with planar density due to the Smoluchowski smoothing phenomenon.[68] Surface electrons tend to redistribute themselves to smooth out abrupt changes in potential at the atomic scale. This redistribution causes an accumulation of electron density in lower coordinated regions. This smoothing reduces the surface dipole moment, especially on rough or low-density surfaces, leading to a lower work function. Conversely, on smoother or more densely packed surfaces where electron smoothing is less pronounced, the surface dipole remains stronger, resulting in a higher work function. The planar density in atoms/Å^2 can be calculated as

$$\text{Planar Density} = N_s/A_s \quad (4)$$

where N_s is the number of atoms on the surface and A_s is the area of the surface.

In our case, for all MXenes, the number of atoms on the surface is the same, i.e. four O atoms. The only remaining variable is A_s. The Φ is inversely proportional to the surface area. However, for systems that we used dipole correction, that is, nonsymmetric MXenes, the trend is linear only when we consider the average of Φ. The trend is not perfectly linear because we are comparing surfaces with different compositions. Therefore, the nature of the chemical element also influences the value of Φ, which impacts the value of the coefficient of determination (R^2), which is not equal to unity.

In the following, we compare our results with other theoretical or experimental data. However, Φ results for our specific MXenes compositions and calculation settings are scarce in the literature. Hence, our comparisons in many cases will be for similar MXenes. For $Nb_4C_3O_2$, our results do not match the values of the work of Xin and Yu.[59] In their work, they used a different approach to dispersion corrections. For Nb_2CO_x, literature results found 5.04 eV; however, the number of layers is different from our work, which makes the comparison difficult.[69] For Mo_2CO_2, the difference between our work and literature may be attributed to different functional.[56,59] In the case of $Ti_3C_2O_2$, our calculated value is close to other theoretical works but different from experiments (4.85 eV) due to F terminations; that is, the experimental value is larger due to the high electronegativity of F.[70−72] Terminations that have electronegativities lower than those of the bare surface decrease the Φ, while those with higher electronegativities have the opposite effect. This phenomenon is interpreted as follows: higher electronegative species harvest electrons from the surface of the material, which reduce the Fermi level.

3.7. Electron Localization Function Analysis. To further characterize our MXenes, we investigated the nature of the chemical bond. For that, we calculated the electron localization function (ELF),[73] which measures the probability density of finding another electron near the reference electron. In this analysis, values closer to unity between atoms indicate complete localization (covalent bonds). Values close to zero between the atoms indicate no localization (ionic bonds). The ELF is calculated using the following equation:

$$\text{ELF} = \frac{1}{1 + \chi(\mathbf{r})} \quad (5)$$

where $\chi(\mathbf{r})$ is the ratio of electron localization to the uniform electron gas.

In MXenes, it is known that the metal t_{2g}-states overlap with the X and T p-states leading to the π-bonds; however, the lower-lying bonding e_g-states form strong directional σ-bonds

https://doi.org/10.1021/acsomega.5c04416
ACS Omega 2025, 10, 32310−32325

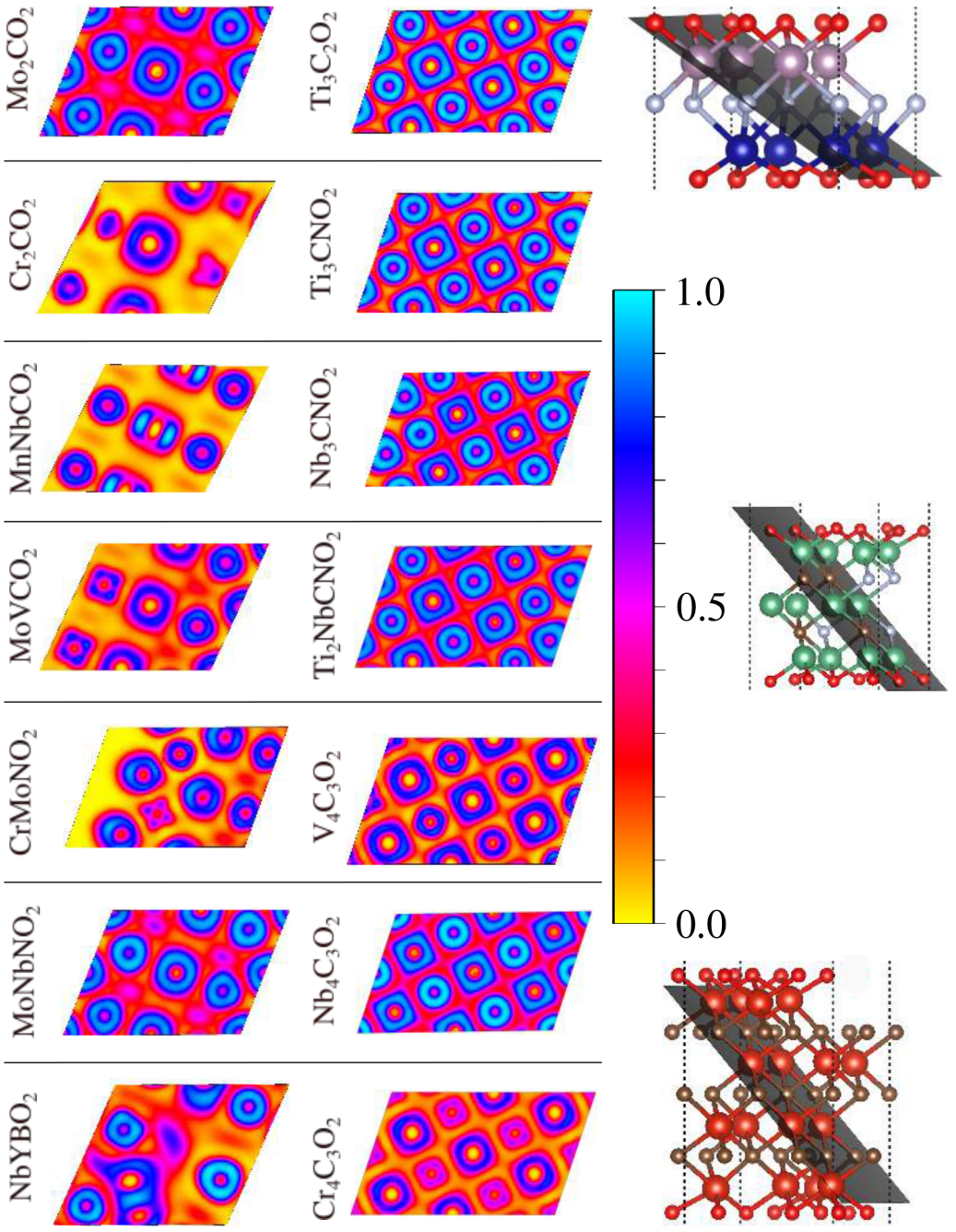

Figure 7. Two-dimensional projection of electron localization function for lowest energy structures. We considered the layer with the maximum number of bonds.

with the *s*- and *p*-states of the *X* and *T* elements.[4,63] Figure 7 shows that most MXenes have some ionic character, i.e., localization in atoms and smaller localization between the atoms. Some systems are more ionic than others, namely Cr_2CO_2, $MnNbCO_2$, $MoVCO_2$, $CrMoNO_2$ and $NbYBO_2$, where we observed the localization of electrons in the atoms (ELF≈ 1) and no localization between the atoms (ELF≈ 0), indicating a high ionic character. The other systems have bonds with smaller ionic character.

3.8. Density of States Characterization. We calculated the DOS of the lowest energy structures to complement the results of band structure calculations (see below). The DOS allows us to observe, for example, which materials can become semiconductors if calculated with the hybrid functional. This analysis is important because metallic materials are more suitable for electrochemical applications.[74] Before discussing our results, we highlight that the PBE usually underestimates E_g due to incomplete cancellation of the self-interaction error.[75] This issue is partially corrected by Hubbard corrections. Regarding the effect of vdW corrections on the E_g of MXenes, we have one systematic study of Ontiveros et al., which showed that both DFT and DFT-D3 underestimate the E_g for the MXenes Zr_2CO_2, $HfCO_2$, $ScCO_2$, Y_2NO_2, W_2NO_2 and Mo_2NO_2.[76] For other materials, other literature works led to the same conclusions; e.g., Torres et al. and Barhoumi and Said demonstrated that the E_g for TiO_2, Ti_2O_3 and bismuth oxyhalides is underestimated by DFT and DFT-vdW framework.[77,78]

https://doi.org/10.1021/acsomega.5c04416
ACS Omega 2025, 10, 32310−32325

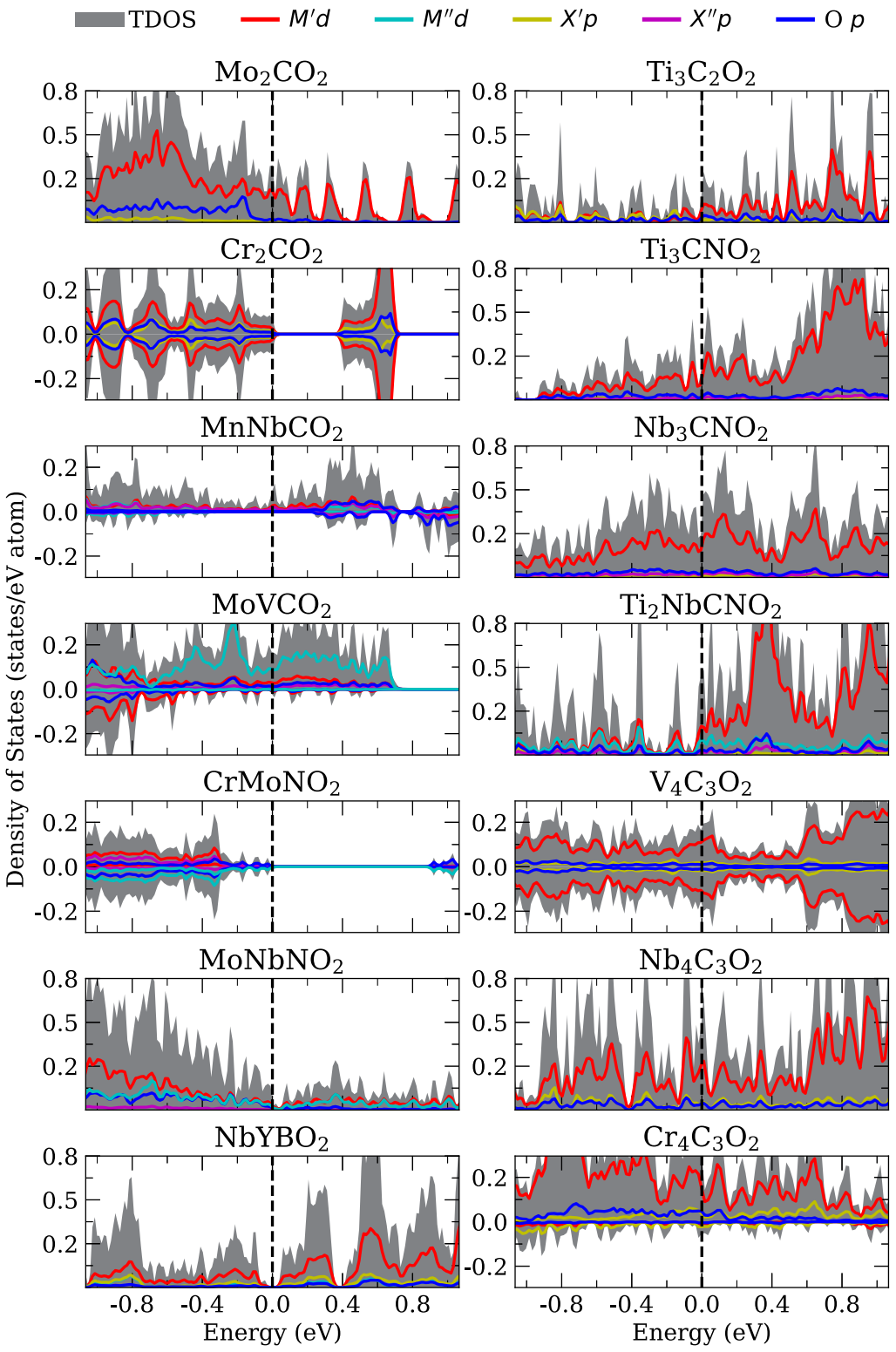

Figure 8. Average total (TDOS) and projected density of states for lowest energy structures. We used a Gaussian broadening of 0.01 eV. The vertical black dashed lines indicate the Fermi level.

Figure 8 shows that most of our MXenes are metallic. The systems $MnNbCO_2$, $MoNbNO_2$, $Ti_3C_2O_2$, and Ti_3CNO_2 have a small DOS at or near the Fermi level, which may result in a band gap when calculated with hybrid functionals. The results of the literature show that, with the HSE calculations, Cr_2CO_2 is a magnetic semiconductor.[39,79] The literature reports also show that V_4C_3 (no termination group) and $Nb_4C_3O_2$ are metallic, according to our results.[80,81] For other systems, we lack experimental or theoretical results for comparison. The other metallic systems exhibit a high DOS near the Fermi level, which suggests that they are likely metallic, even when using other functionals. The *d*-states of the metal contribute predominantly to the DOS near the Fermi level.

https://doi.org/10.1021/acsomega.5c04416
ACS Omega 2025, 10, 32310−32325

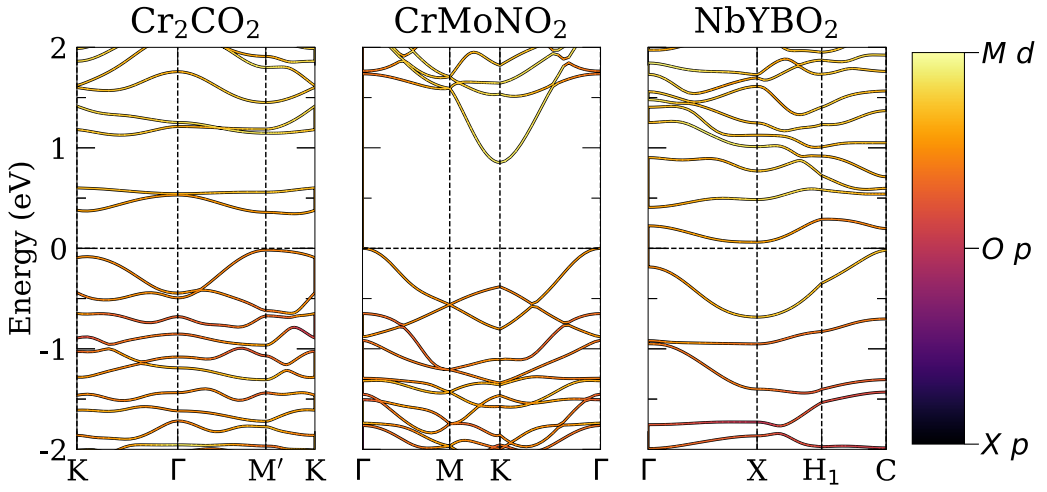

Figure 9. Band structure for the lowest energy structure of semiconductor MXenes. The horizontal black dashed lines indicate the VBM, obtained from a calculation with **k**-mesh doubled. For the color coding, we considered the general formula $(M'M'')_{n+1}(X'X'')_nO_2$ and for MXenes with two different metals or *X* elements, we summed the contributions. The paths are in accordance with the work of Wang et al.[82]

3.9. Band Structure of Semiconductor MXenes. We calculated the band structure of the lowest energy structures to understand the metallic or semiconductor nature of our MXenes and complement the DOS calculations. Figure 9 shows the results for semiconductor MXenes. Additional results for band structure and DOS are available in the SI. For all compositions, the electronic states contributions show that the largest contribution for the bands comes from the metal *d*-states, then oxygen *p*-states, and finally *p*-states from *X* elements. The majority of our MXenes are metallic with parabolic dispersion near the Fermi level.

The semiconductor systems are Cr_2CO_2 (direct E_g), $CrMoNO_2$ (indirect), and $NbYBO_2$ (indirect). The E_g is larger for Cr_2CO_2 and $CrMoNO_2$; see Table 2. The E_g is directly proportional to the ionic character of the bond between metals and anions. The thermodynamic electronegativity of nitrogen (3.56) is higher than that of boron (3.04), and the sum of the electronegativity of Cr (2.12) and Mo (2.47) is lower than the sum of Nb (2.59) and Y (2.52).[83] Therefore, the bonds Cr_2CO_2 and $CrMoNO_2$ are more ionic, resulting in a larger electronic E_g. The metallic system $MnNbCO_2$ has a bandgap for one spin component, which opens possibilities for spintronics applications, see SI.

These results are in accordance with the ELF discussion; e.g., most systems have a small ionic character, which results in a metallic nature. For Cr_2CO_2 and $CrMoNO_2$, bonds are predominantly ionic, which implies a relatively large E_g. For $NbYBO_2$, the ionic character is smaller, resulting in a smaller electronic E_g. Note that the bonds in other systems have some ionic character; however, it is not enough to result in a semiconductor nature. Other literature works have shown that the character of the *M*-*X* and *M*-*T* bonds determines the E_g, e.g., the larger the ionic character, the larger the E_g. The ionic character is smaller for less electronegative ligands, e.g., C < *N* < O and also decreases with the number of *d*-electrons.[4,63,64] Metallic interactions occur for long-range $t_{2g} - t_{2g}$ overlap, which is larger for metals with many *d* electrons. We should highlight that other mechanisms can be involved in the magnitude of the E_g, e.g., shifting of the Fermi energy to the center of the gap between the *M d*- and *X p*-states due to mixing of these states upon functionalization.[84]

4. INSIGHTS INTO MXENES APPLICATIONS

The values of Φ are an important parameter for practical applications of MXenes in catalysis,[67] electrochemistry,[74] photodetection,[85] and energy conversion.[69] We observed the lowest Φ values for $NbYBO_2$ and $Nb_4C_3O_2$ and the highest Φ values for Mo_2CO_2 and Cr_2CO_2. In catalysis, this quantity is important because adsorbates that have electronegativities lower than those of the substrate atoms typically decrease the Φ, while those with higher electronegativities have the opposite effect.[67] This phenomenon is interpreted as follows: higher electronegative species harvest electrons from the surface of the material, which reduces the Fermi level.

In electrochemistry, MXenes with lower Φ values lose electrons easier and can be used in HER, nitrogen reduction, CO_2 reduction, or other redox reactions.[74,86] For example, Gui et al. modified $Ti_3C_2T_x$ with Fe, which greatly reduced the Φ. The MXene/$TiFeO_x$ achieved a Faradaic efficiency of 25.44% and NH_3 yield larger than all reported MXene-based materials for nitrogen reduction.[87] Chen et al. studied $Ti_3C_2T_x$ for photodetection applied to image sensing. In this area, materials with lower Φ are used to collect electrons, and the ones with higher Φ will be used to collect holes.[85] The authors were able to synthesize $Ti_3C_2T_x$ with few defects, which finally enhanced the efficiency of the optoelectronic device.

In energy conversion, Zhang et al. applied Nb_2CT_x MXene as the hole transport layer for perovskite solar cells.[69] Nb_2CT_x was chosen because it has a larger surface area in comparison with $Ti_3C_2T_x$. In their work, they demonstrated that treating MXene with oxygen plasma increased the number of oxygen terminations, causing an increase in Φ due to the high electronegativity of oxygen. In the case of perovskite solar cells, the increase in Φ is important because it decreases the recombination of charges. This led to an increase in the hole transfer efficiency in the perovskite/MXene interface. Their final material was stable and achieved a power conversion efficiency of 20.74%. The authors also highlight the flexibility of MXenes, which is another important feature of solar cells for flexible devices. In addition, Φ can be further tuned with other terminations.

https://doi.org/10.1021/acsomega.5c04416
ACS Omega 2025, 10, 32310−32325

5. CONCLUSIONS

In this work, we investigated the compositions of 14 MXenes with a different number of layers using the PBE and PBE + U approximations. We extensively explored the structure space, including fcc and hcp terminations, o^M-MXenes, i^M-MXenes, o^X-MXenes, i^X-MXenes, NM, FM, FIM, and AFM configurations. After 240 stress-tensor calculations, we selected the lowest energy structure to calculate cohesive energies, band structures, density of states, work function, nominal charges, electron localization function, and DDEC6 charge analysis.

Our results from PBE calculations showed that most systems are NM for all configurations in the structure space, namely Mo_2CO_2, $MoNbNO_2$, $NbYBO_2$, $Ti_3C_2O_2$, Ti_3CNO_2, Nb_3CNO_2, Ti_2NbCNO_2, and $Nb_4C_3O_2$. This is expected because O binds to d electrons, which hinders magnetism. Our PBE and PBE + U analysis shows that, for systems with Cr, Mn, V the inclusion of U leads to important differences. For $MnNbCO_2$ and $V_4C_3O_2$, both functionals agree in terms of T site preference, however, there are important differences regarding a_0 and magnetic properties. For Cr_2CO_2, $CrMoNO_2$, and $Cr_4C_3O_2$, the differences between both functionals are more critical, that is, even the predicted T site changes. For $MoVCO_2$, the differences between both functionals are marginal, with only an enhancement of local magnetic moments.

Our results of the cohesive energies showed that most MXenes prefer fcc terminations, while hcp minimized the energy for Mo_2CO_2, $CrMoNO_2$, $MoVCO_2$ (Mo side), and $MoNbNO_2$. For double-metal MXenes, in-plane configuration is more stable for $MnNbCO_2$, $MoNbNO_2$, $NbYBO_2$, Ti_3CNO_2, and Nb_3CNO_2, while the out-of-plane structure minimized the energy for $MoVCO_2$, $CrMoNO_2$, and Ti_2NbCNO_2. Therefore, theoretical calculations, even when focused on specific applications of MXenes, should explore the structural space to identify the lowest energy configuration. This is particularly important for double-metal MXenes, where most of the literature studies assume the structure of o^M-MXene. This assumption is unjustified and may result in the identification of an incorrect energy minimum. The same conclusion is valid for double X MXenes. Interestingly, the lowest energy structure of $NbYBO_2$ showed an unexpected structure with migration of the boron atom site. These results and the lack of experimental data for MBenes indicate that these materials should be further explored. A similar X site migration occurs for Cr_2CO_2.

Regarding structural features, the preference for the hcp or fcc termination site is explained by LFT and the number of nonbonding electrons, which is in agreement with the majority of DDEC6 charge analysis. Our analysis of d-states occupancy further showed that the d_{z^2} occupancy is correlated with the termination site. However, explaining the configurations of o^M-MXenes, i^M-MXenes, o^X-MXenes, or i^X-MXenes is beyond the scope of LFT, which implies again that structure space exploration is essential for obtaining meaningful theoretical results.

As expected, the majority of our compositions are metallic, which is advantageous for applications of these materials as electrodes, e.g., in electrochemistry applications. In these applications, metals are favorable because there is no bandgap and a large concentration of electrons on the surface. Thus, the application of a potential can result in electron transference to adsorbates more easily than in semiconductors.[74]

For the systems $MnNbCO_2$, $MoNbNO_2$, $Ti_3C_2O_2$, and Ti_3CNO_2, we observed a small density of states near the Fermi level. Depending on the desired application, the band gap of these two systems should be further investigated theoretically or experimentally. Finally, our calculated work functions are within a range of 3.75−7.42 eV, which is explained by surface area and compositions. We emphasize how information about work functions can be used to guide MXene applications. Therefore, our results can aid experimentalists in practical applications and theoretical scientists in future studies.

■ ASSOCIATED CONTENT

Data Availability Statement

The authors declare no competing financial interest. As mentioned, all DFT calculations were done using the VASP package, which can be used under a nonfree academic license. Furthermore, additional details are provided within the SI, while additional raw data can be obtained directly from the authors upon request. We also provide the data in the Mendeley Data Repository, where it is listed under the same title as this work.

Supporting Information

The Supporting Information is available free of charge at https://pubs.acs.org/doi/10.1021/acsomega.5c04416.

Additional technical details, further computational methodologies, in-depth convergence calculations, and complete set of equilibrium lattice parameters and electronic properties for all systems (PDF)

■ AUTHOR INFORMATION

Corresponding Author

Juarez L. F. Da Silva − *São Carlos Institute of Chemistry, University of São Paulo, 13560-970 São Carlos, SP, Brazil;* orcid.org/0000-0003-0645-8760; Email: juarez_dasilva@iqsc.usp.br

Authors

Mauricio Mocelim − *São Carlos Institute of Chemistry, University of São Paulo, 13560-970 São Carlos, SP, Brazil;* orcid.org/0000-0002-4683-7223

Henrique A. B. Fonseca − *São Carlos Institute of Chemistry, University of São Paulo, 13560-970 São Carlos, SP, Brazil*

Pedro Ivo R. Moraes − *São Carlos Institute of Chemistry, University of São Paulo, 13560-970 São Carlos, SP, Brazil;* orcid.org/0000-0001-7339-5945

Complete contact information is available at: https://pubs.acs.org/10.1021/acsomega.5c04416

Funding

The Article Processing Charge for the publication of this research was funded by the Coordenacao de Aperfeicoamento de Pessoal de Nivel Superior (CAPES), Brazil (ROR identifier: 00x0ma614).

Notes

The authors declare no competing financial interest.

■ ACKNOWLEDGMENTS

The authors appreciate the support from FAPESP (São Paulo Research Foundation) and Shell, project numbers 2017/11631−2 and 2018/21401−7 and the strategic importance of the support provided by ANP (Brazil's National Oil, Natural Gas and Biofuels Agency). The authors also thank the

infrastructure provided to our computer cluster by the Department of Information Technology − Campus São Carlos. M.M., P.I.R.M. and H.A.B.F. acknowledge FAPESP for financial support, grant numbers 2023/15357−3, 2023/12824−0, and 2021/05728−9. We acknowledge the use of advanced language models for their assistance in English-language editing, grammar revision, and text refinement.

■ ABBREVIATION

DFT: Density functional theory; VASP: Vienna ab initio simulation package; PBE: Perdew−Burke−Ernzerhof; PAW: Projector augmented-wave

■ REFERENCES

(1) Gogotsi, Y.; Anasori, B. The Rise of MXenes. *ACS Nano* **2019**, *13*, 8491−8494.
(2) Lim, K. R. G.; Shekhirev, M.; Wyatt, B. C.; Anasori, B.; Gogotsi, Y.; Seh, Z. W. Fundamentals of MXene Synthesis. *Nat. Synth.* **2022**, *1*, 601−614.
(3) Li, X.; Huang, Z.; Shuck, C. E.; Liang, G.; Gogotsi, Y.; Zhi, C. MXene Chemistry, Electrochemistry and Energy Storage Applications. *Nat. Rev. Chem.* **2022**, *6*, 389−404.
(4) Bera, S.; Kumar, H. Phase Stability of MXenes: Understanding the Role of Coordination Symmetries, Transition Metals, and Surface Terminations. *J. Phys. Chem. C* **2023**, *127*, 20734−20741.
(5) Lee, E.; VahidMohammadi, A.; Yoon, Y. S.; Beidaghi, M.; Kim, D.-J. Two-Dimensional Vanadium Carbide MXene for Gas Sensors with Ultrahigh Sensitivity Toward Nonpolar Gases. *ACS Sens.* **2019**, *4*, 1603−1611.
(6) Dall'Agnese, Y.; Taberna, P.-L.; Gogotsi, Y.; Simon, P. Two-Dimensional Vanadium Carbide (MXene) as Positive Electrode for Sodium-Ion Capacitors. *J. Phys. Chem. Lett.* **2015**, *6*, 2305−2309.
(7) Zhang, J.; Huang, C.; Sun, Y.; Yu, H. Amino-Functionalized Niobium-Carbide MXene Serving as Electron Transport Layer and Perovskite Additive for the Preparation of High-Performance and Stable Methylammonium-Free Perovskite Solar Cells. *Adv. Funct. Mater.* **2024**, *32*, No. 2113367.
(8) Deeva, E.; Kurlov, A.; Abdala, P. M.; Lebedev, D.; Kim, S. M.; Gordon, C. P.; Tsoukalou, A.; Fedorov, A.; Müller, C. R. In Situ XANES/XRD Study of the Structural Stability of Two-Dimensional Molybdenum Carbide Mo_2CT_x: Implications for the Catalytic Activity in the Water−Gas Shift Reaction. *Chem. Mater.* **2019**, *31*, 4505−4513.
(9) Seh, Z. W.; Fredrickson, K. D.; Anasori, B.; Kibsgaard, J.; Strickler, A. L.; Lukatskaya, M. R.; Gogotsi, Y.; Jaramillo, T. F.; Vojvodic, A. Two-Dimensional Molybdenum Carbide (MXene) as an Efficient Electrocatalyst for Hydrogen Evolution. *ACS Energy Lett.* **2016**, *1*, 589−594.
(10) Zheng, J.; Sun, X.; Qiu, C.; Yan, Y.; Yao, Z.; Deng, S.; Zhong, X.; Zhuang, G.; Wei, Z.; Wang, J. High-Throughput Screening of Hydrogen Evolution Reaction Catalysts in MXene Materials. *J. Phys. Chem. C* **2020**, *124*, 13695−13705.
(11) VahidMohammadi, A.; Rosen, J.; Gogotsi, Y. The World of Two-dimensional Carbides and Nitrides (MXenes). *Science* **2021**, *372*, No. eabf1581.
(12) Naguib, M.; Barsoum, M. W.; Gogotsi, Y. Ten Years of Progress in the Synthesis and Development of MXenes. *Adv. Mater.* **2024**, *33*, No. 2103393.
(13) Gogotsi, Y.; Huang, Q. MXenes: Two-Dimensional Building Blocks for Future Materials and Devices. *ACS Nano* **2021**, *15*, 5775−5780.
(14) Urbankowski, P.; Anasori, B.; Hantanasirisakul, K.; Yang, L.; Zhang, L.; Haines, B.; May, S. J.; Billinge, S. J. L.; Gogotsi, Y. 2D Molybdenum and Vanadium Nitrides Synthesized by Ammoniation of 2D Transition Metal Carbides (MXenes). *Nanoscale* **2017**, *9*, 17722−17730.
(15) Yoon, Y.; Tiwari, A. P.; Lee, M.; Choi, M.; Song, W.; Im, J.; Zyung, T.; Jung, H.-K.; Lee, S. S.; Jeon, S.; An, K.-S. Enhanced Electrocatalytic Activity by Chemical Nitridation of Two-dimensional Titanium Carbide MXene for Hydrogen Evolution. *J. Mater. Chem. A* **2018**, *6*, 20869−20877.
(16) Li, N.; Zeng, Z.; Zhang, Y.; Chen, X.; Kong, Z.; Arramel; Li, Y.; Zhang, P.; Nguyen, B.-S. Double Transition Metal Carbides MXenes (D-MXenes) as Promising Electrocatalysts for Hydrogen Reduction Reaction: Ab Initio Calculations. *ACS Omega* **2021**, *6*, 23676−23682.
(17) Abraham, B. M.; Sinha, P.; Halder, P.; Singh, J. K. Fusing a Machine Learning Strategy with Density Functional Theory to Hasten the Discovery of 2D MXene-based Catalysts for Hydrogen Generation. *J. Mater. Chem. A* **2023**, *11*, 8091−8100.
(18) Liu, W.; Cao, J.; Song, F.; Zhang, D.-D.; Okhawilai, M.; Yi, J.; Qin, J.-Q.; Zhang, X.-Y. A Double Transition Metal Ti_2NbC_2Tx MXene for Enhanced Lithium-Ion Storage. *Rare Met.* **2023**, *42*, 100−110.
(19) Du, Z.; Wu, C.; Chen, Y.; Zhu, Q.; Cui, Y.; Wang, H.; Zhang, Y.; Chen, X.; Shang, J.; Li, B.; Chen, W.; Liu, C.; Yang, S. High-Entropy Carbonitride MAX Phases and Their Derivative MXenes. *Adv. Energy Mater.* **2022**, *12*, No. 2103228.
(20) Huang, B.; Zhou, N.; Chen, X.; Ong, W.-J.; Li, N. Insights into the Electrocatalytic Hydrogen Evolution Reaction Mechanism on Two-Dimensional Transition-Metal Carbonitrides (MXene). *Chem.—Eur. J.* **2018**, *24*, 18479−18486.
(21) Zeng, Z.; Chen, X.; Weng, K.; Wu, Y.; Zhang, P.; Jiang, J.; Li, N. Computational Screening Study of Double Transition Metal Carbonitrides M′ 2M″CNO_2-MXene as Catalysts for Hydrogen Evolution Reaction. *npj Comput. Mater.* **2021**, *7*, 1−7.
(22) Cheng, Y.; Wang, L.; Song, Y.; Zhang, Y. Deep Insights Into the Exfoliation Properties of MAX to MXenes and the Hydrogen Evolution Performances of 2D MXenes. *J. Mater. Chem. A* **2019**, *7*, 15862−15870.
(23) Zou, X.; Liu, H.; Xu, H.; Wu, X.; Han, X.; Kang, J.; Reddy, K. M. A Simple Approach to Synthesis Cr_2CT_x MXene for Efficient Hydrogen Evolution Reaction. *Mater. Today Energy* **2021**, *20*, No. 100668.
(24) Jiang, Y.; Sun, T.; Xie, X.; Jiang, W.; Li, J.; Tian, B.; Su, C. Oxygen-Functionalized Ultrathin $Ti_3C_2T_x$ MXene for Enhanced Electrocatalytic Hydrogen Evolution. *ChemSusChem* **2019**, *12*, 1368−1373.
(25) Cao, D.; Liu, H.; Sun, Q.; Wang, X.; Wang, J.; Liu, C.; Liu, C.; Hao, Q.; Li, Y. Tailoring the Electronic Structure by Transition-metal Single Atom on $Ti_3C_2O_2$ for Improving Hydrogen Evolution Activity. *Appl. Surf. Sci.* **2021**, *563*, No. 150210.
(26) Tran, M. H.; Schäfer, T.; Shahraei, A.; Dürrschnabel, M.; Molina-Luna, L.; Kramm, U. I.; Birkel, C. S. Adding a New Member to the MXene Family: Synthesis, Structure, and Electrocatalytic Activity for the Hydrogen Evolution Reaction of $V_4C_3T_x$. *ACS Appl. Energy Mater.* **2018**, *1*, 3908−3914.
(27) Tan, Y.; Zhu, Z.; Zhang, X.; Zhang, J.; Zhou, Y.; Li, H.; Qin, H.; Bo, Y.; Pan, Z. $Nb_4C_3T_x$ (MXene) as a New Stable Catalyst for the Hydrogen Evolution Reaction. *Int. J. Hydrogen Energy* **2021**, *46*, 1955−1966.
(28) Šljivančanin, Ž. Optimizing Hydrogen Evolution Reaction: Computational Screening of Single Metal Atom Impurities in 2D MXene $Nb_4C_3O_2$. *Front. Phys.* **2024**, *19*, 1−8.
(29) Pandey, M.; Thygesen, K. S. Two-Dimensional MXenes as Catalysts for Electrochemical Hydrogen Evolution: A Computational Screening Study. *J. Phys. Chem. C* **2017**, *121*, 13593−13598.
(30) Hope, M. A.; Forse, A. C.; Griffith, K. J.; Lukatskaya, M. R.; Ghidiu, M.; Gogotsi, Y.; Grey, C. P. NMR Reveals the Surface Functionalisation of Ti_3C_2 MXene. *Phys. Chem. Chem. Phys.* **2016**, *18*, 5099−5102.
(31) Handoko, A. D.; Fredrickson, K. D.; Anasori, B.; Convey, K. W.; Johnson, L. R.; Gogotsi, Y.; Vojvodic, A.; Seh, Z. W. Tuning the Basal Plane Functionalization of Two-Dimensional Metal Carbides (MXenes) To Control Hydrogen Evolution Activity. *ACS Appl. Energy Mater.* **2018**, *1*, 173−180.
(32) Hohenberg, P.; Kohn, W. Inhomogeneous Electron Gas. *Phys. Rev.* **1964**, *136*, B864−B871.

https://doi.org/10.1021/acsomega.5c04416
ACS Omega 2025, 10, 32310−32325

(33) Kohn, W.; Sham, L. J. Self-consistent Equations Including Exchange and Correlation Effects. *Phys. Rev.* **1965**, *140*, A1133−A1138.
(34) Kresse, G.; Hafner, J. *Ab initio* Molecular Dynamics for Open-shell Transition Metals. *Phys. Rev. B* **1993**, *48*, 13115−13118.
(35) Grimme, S.; Antony, J.; Ehrlich, S.; Krieg, H. A Consistent and Accurate ab Initio Parametrization of Density Functional Dispersion Correction (DFT-D) for the 94 Elements H-Pu. *J. Chem. Phys.* **2010**, *132*, 154104.
(36) Tran, F.; Stelzl, J.; Blaha, P. Rungs 1 to 4 of DFT Jacob's ladder: Extensive Test on The Lttice Constant, Bulk Modulus, and Cohesive Energy of Solids. *J. Chem. Phys.* **2016**, *144*, 204120.
(37) Peng, H.; Perdew, J. P. Rehabilitation of the Perdew-Burke-Ernzerhof Generalized Gradient Approximation for Layered Materials. *Phys. Rev. B* **2017**, *95*, No. 081105.
(38) Perdew, J. P.; Burke, K.; Ernzerhof, M. Generalized Gradient Approximation Made Simple. *Phys. Rev. Lett.* **1996**, *77*, 3865−3868.
(39) Tan, Z.; Fang, Z.; Li, B.; Yang, Y. First-Principles Study of the Ferromagnetic Properties of Cr_2CO_2 and Cr_2NO_2 MXenes. *ACS Omega* **2020**, *5*, 25848−25853.
(40) Musa Saad, H.-E. M.; Alsobhi, B. O. A Comprehensive GGA Investigation on the Structural, Elastic, Electronic, and Magnetic Properties of Vanadium-Based Half-Heusler XVZ (X = Cr, Mn, Fe; Z = Sn, Sb) Compounds. *J. Electron. Mater.* **2023**, *52*, 4738−4755.
(41) Xie, Y.; Kent, P. R. C. Hybrid Density Functional Study of Structural and Electronic Properties of Functionalized $Ti_{n+1}X_n$ (X = C, N) Monolayers. *Phys. Rev. B* **2013**, *87*, No. 235441.
(42) Chibani, H.; Yahi, H.; Arshad, N.; Ouettar, C. Revealing Structural, Mechanical, and Electronic Properties of M_4C_3 (M = Sc, Ti, Zr, Mo, Hf, and W) MXene Monolayers Based on First-principle Calculations. *Comput. Condens. Matter* **2022**, *32*, No. e00713.
(43) Dudarev, S. L.; Botton, G. A.; Savrasov, S. Y.; Humphreys, C. J.; Sutton, A. P. Electron-Energy-Loss Spectra and the Structural Stability of Nickel Oxide: An LSDA+U Study. *Phys. Rev. B* **1998**, *57*, 1505−1509.
(44) Blöchl, P. E. Projector Augmented-Wave Method. *Phys. Rev. B* **1994**, *50*, 17953−17979.
(45) Kresse, G.; Joubert, D. From Ultrasoft Pseudopotentials to the Projector Augmented-wave Method. *Phys. Rev. B* **1999**, *59*, 1758−1775.
(46) Zhao, Z.; Qian, X.; Zhu, H.; Miao, Y.; Ye, H. Synthesis of Accordion-like Ti_3CN MXene and its Structural Stability in Aqueous Solutions and Organic Solvents. *ChemistrySelect* **2022**, *7*, No. e202104176.
(47) Guo, Y.; Zhang, X.; Jin, S.; Xia, Q.; Chang, Y.; Wang, L.; Zhou, A. Synthesis of Mo_2C MXene with High Electrochemical Performance by Alkali Hydrothermal Etching. *J. Adv. Ceram.* **2023**, *12*, 1889−1901.
(48) Han, M.; Maleski, K.; Shuck, C. E.; Yang, Y.; Glazar, J. T.; Foucher, A. C.; Hantanasirisakul, K.; Sarycheva, A.; Frey, N. C.; May, S. J.; Shenoy, V. B.; Stach, E. A.; Gogotsi, Y. Tailoring Electronic and Optical Properties of MXenes through Forming Solid Solutions. *J. Am. Chem. Soc.* **2020**, *142*, 19110−19118.
(49) Pinto, D.; Anasori, B.; Avireddy, H.; Shuck, C. E.; Hantanasirisakul, K.; Deysher, G.; Morante, J. R.; Porzio, W.; Alshareef, H. N.; Gogotsi, Y. Synthesis and Electrochemical Properties of 2D Molybdenum Vanadium Carbides−Solid Solution MXenes. *J. Mater. Chem. A* **2020**, *8*, 8957−8968.
(50) Gouveia, J. D.; Viñes, F.; Illas, F.; Gomes, J. R. B. MXenes Atomic Layer Stacking Phase Transitions and Their Chemical Activity Consequences. *Phys. Rev. Mater.* **2020**, *4*, No. 054003.
(51) Deysher, G.; Shuck, C. E.; Hantanasirisakul, K.; Frey, N. C.; Foucher, A. C.; Maleski, K.; Sarycheva, A.; Shenoy, V. B.; Stach, E. A.; Anasori, B.; Gogotsi, Y. Synthesis of Mo_4VAlC_4 MAX Phase and Two-Dimensional Mo_4VC_4 MXene with Five Atomic Layers of Transition Metals. *ACS Nano* **2020**, *14*, 204−217.
(52) Wang, X.; Lin, S.; Tong, H.; Huang, Y.; Tong, P.; Zhao, B.; Dai, J.; Liang, C.; Wang, H.; Zhu, X.; Sun, Y.; Dou, S. Two-dimensional V_4C_3 MXene as High Performance Electrode Materials for Supercapacitors. *Electrochim. Acta* **2019**, *307*, 414−421.
(53) Huang, B.; Li, N.; Ong, W.-J.; Zhou, N. Single Atom-supported MXene: How Single-atomic-site Catalysts Tune the High Activity and Selectivity of Electrochemical Nitrogen Fixation. *J. Mater. Chem. A* **2019**, *7*, 27620−27631.
(54) Bury, D.; Jakubczak, M.; Purbayanto, M. A. K.; Rybak, M.; Birowska, M.; Wójcik, A.; Moszczyńska, D.; Eisawi, K.; Prenger, K.; Presser, V.; Naguib, M.; Jastrzebska, A. M. Wet-Chemical Etching and Delamination of MoAlB into MBene and Its Outstanding Photocatalytic Performance. *Adv. Funct. Mater.* **2023**, *33*, No. 2308156.
(55) Hayat, A.; Bashir, T.; Ahmed, A. M.; Ajmal, Z.; Alghamdi, M. M.; El-Zahhar, A. A.; Sohail, M.; Amin, M. A.; Al-Hadeethi, Y.; Ghasali, E.; Raza, S.; Orooji, Y. Novel 2D MBenes-synthesis, Structure, Properties with Excellent Performance in Energy Conversion and Storage: A Review. *Materials Science and Engineering: R: Reports* **2024**, *159*, No. 100796.
(56) Wan, P.; Tang, Q. The Effect of Constant Potential on the Hydrogen Evolution Reaction Activity of M_2CO_2 and M_2NO_2 MXenes. *ChemPhysChem* **2023**, *24*, No. e202200871.
(57) Li, L. Lattice Dynamics and Electronic Structures of $Ti_3C_2O_2$ and $Mo_2TiC_2O_2$ (MXenes): The Effect of Mo Substitution. *Comput. Mater. Sci.* **2016**, *124*, 8−14.
(58) Wang, Z.; Di, H.; Sun, R.; Zhu, Y.; Yin, L.; Zhang, Z.; Wang, C. Electrocatalytic Hydrogen Evolution Performance of Modified $Ti_3C_2O_2$ Doped with Non-metal Elements: A DFT Study. *ChemPhysMater.* **2022**, *1*, 321−329.
(59) Xin, Y.; Yu, Y.-X. Possibility of Bare and Functionalized Niobium Crbide MXenes for Electrode Materials of Supercapacitors and Field Emitters. *Mater. Des.* **2017**, *130*, 512−520.
(60) Plummer, G.; Thomas, S.; Asle Zaeem, M.; Tucker, G. J. Bond-order Potential for the Surface-Terminated Titanium Carbide MXene Monolayers $Ti_{n+1}C_nT_x$ (n = 1,2 or 3; T=−O or −F). *Phys. Rev. B* **2022**, *106*, No. 054105.
(61) Khazaei, M.; Arai, M.; Sasaki, T.; Chung, C.-Y.; Venkataramanan, N. S.; Estili, M.; Sakka, Y.; Kawazoe, Y. Novel Electronic and Magnetic Properties of Two-Dimensional Transition Metal Carbides and Nitrides. *Adv. Funct. Mater.* **2013**, *23*, 2185−2192.
(62) Sarmah, H. S.; Ghosh, S. In-plane Ordering and Tunable Magnetism in Cr-based MXenes. *arXiv* **2024**.
(63) Rosenkranz, A.; Righi, M. C.; Sumant, A. V.; Anasori, B.; Mochalin, V. N. Perspectives of 2D MXene Tribology. *Adv. Mater.* **2023**, *35*, No. 2207757.
(64) Amargianou, F.; Bärmann, P.; Shao, H.; Taberna, P.-L.; Simon, P.; Gonzalez-Julian, J.; Weigand, M.; Petit, T. Nanoscale Surface and Bulk Electronic Properties of $Ti_3C_2T_x$ MXene Unraveled by Multimodal X-Ray Spectromicroscopy. *Small. Methods* **2024**, *8*, No. 2400190.
(65) Bader, R. F. W. *Atoms in Molecules: A Quantum Theory*; International Series of Monographs on Chemistry; Clarendon Press, 1994.
(66) Manz, T. A.; Limas, N. G. Introducing DDEC6 Atomic Population Analysis: Part 1. Charge Partitioning Theory and Methodology. *RSC Adv.* **2016**, *6*, 47771−47801.
(67) Scheffler, M.; Stampfl, C. Theory of Adsorption on Metal Substrates. In *Electronic Structure*; Horn, K.; Scheffler, M., Eds.; Elsevier BV: Amsterdam, 2000; pp. 285−356.
(68) Smoluchowski, R. Anisotropy of the Electronic Work Function of Metals. *Phys. Rev.* **1941**, *60*, 661−674.
(69) Zhang, J.; Huang, C.; Yu, H. Modulate the Work Function of Nb_2CT_x MXene as the Hole Transport Layer for Perovskite Solar Cells. *Appl. Phys. Lett.* **2021**, *119*, No. 033506.
(70) Schultz, T.; Frey, N. C.; Hantanasirisakul, K.; Park, S.; May, S. J.; Shenoy, V. B.; Gogotsi, Y.; Koch, N. Surface Termination Dependent Work Function and Electronic Properties of $Ti_3C_2T_x$ MXene. *Chem. Mater.* **2019**, *31*, 6590−6597.
(71) Gao, L.; Wang, N.; Cao, J.; Li, Y.; Ma, T. Significant Effect of Base Assisted Intercalates in Synthesis of 2D Semiconductor $Ti_3C_2O_2$. *Surf. Interfaces* **2020**, *20*, No. 100604.

https://doi.org/10.1021/acsomega.5c04416
ACS Omega 2025, 10, 32310−32325

(72) Schultz, T.; Bärmann, P.; Longhi, E.; Meena, R.; Geerts, Y.; Gogotsi, Y.; Barlow, S.; Marder, S. R.; Petit, T.; Koch, N. Work Function and Energy Level Alignment Tuning at $Ti_3C_2T_x$ MXene Surfaces and Interfaces Using (metal-)organic Donor/Acceptor Molecules. *Phys. Rev. Mater.* **2023**, *7*, No. 045002.
(73) Clements, R. J.; Womack, J. C.; Skylaris, C.-K. Electron Localisation Descriptors in ONETEP: A Tool for Interpreting Localisation and Bonding in Large-scale DFT Calculations. *Electron. Struct.* **2020**, *2*, No. 027001.
(74) Peera, S. G.; Koutavarapu, R.; Chao, L.; Singh, L.; Murugadoss, G.; Rajeshkhanna, G. 2D MXene Nanomaterials as Electrocatalysts for Hydrogen Evolution Reaction (HER): A Review. *Micromachines* **2022**, *13*, 1499.
(75) Perdew, J. P. Density Functional Theory and the Band Gap Problem. *Int. J. Quantum Chem.* **1985**, *28*, 497−523.
(76) Ontiveros, D.; Viñes, F.; Sousa, C. Bandgap Engineering of MXene Compounds for Water Splitting. *J. Mater. Chem. A* **2023**, *11*, 13754−13764.
(77) Barhoumi, M.; Said, M. Correction of Band-gap Energy and Dielectric Function of BiO_X Bulk with GW and BSE. *Optik* **2020**, *216*, No. 164631.
(78) Torres, A. E.; Rodríguez-Pineda, J.; Zanella, R. Relevance of Dispersion and the Electronic Spin in the DFT + U Approach for the Description of Pristine and Defective TiO_2 Anatase. *ACS Omega* **2021**, *6*, 23170−23180.
(79) Wei, X.-P.; Yang, N.; Mei, Z.-Y.; Shen, J.; Du, L.-L.; Tao, X. Layer-dependent Electronic and Magnetic Properties for Cr_2NO_2 and Cr_2CO_2. *J. Magn. Magn. Mater.* **2022**, *563*, No. 169952.
(80) Shang, Y.; Han, Y.; Wan, W.; Liu, Y.; Ge, Y. First-principles Study of Two-Dimensional Transition Metal Carbide $M_{n+1}C_nO_2$ (M = Nb,Ta). *J. Phys.: Condens. Matter* **2024**, *36*, 355702.
(81) Sufyan, A.; Abbas, G.; Sajjad, M.; Larsson, J. A. V_4C_3 MXene: a Type-II Nodal Line Semimetal with Potential as High-Performing Anode Material for Mg-Ion Battery. *ChemSusChem* **2024**, *17*, No. e202301351.
(82) Wang, V.; Tang, G.; Liu, Y.-C.; Wang, R.-T.; Mizuseki, H.; Kawazoe, Y.; Nara, J.; Geng, W. T. High-Throughput Computational Screening of Two-Dimensional Semiconductors. *J. Phys. Chem. Lett.* **2022**, *13*, 11581−11594.
(83) Tantardini, C.; Oganov, A. R. Thermochemical Electronegativities of the Elements. *Nat. Commun.* **2021**, *12*, 1−9.
(84) Khazaei, M.; Ranjbar, A.; Arai, M.; Sasaki, T.; Yunoki, S. Electronic Properties and Applications of MXenes: a Theoretical Review. *J. Mater. Chem. C* **2017**, *5*, 2488−2503.
(85) Chen, J.; Liu, X.; Li, Z.; Cao, F.; Lu, X.; Fang, X. Work-Function-Tunable MXenes Electrodes to Optimize p-$CsCu_2I_3$/n-Ca_2Nb_3-TaO_{10} Junction Photodetectors for Image Sensing and Logic Electronics. *Adv. Funct. Mater.* **2022**, *32*, No. 2201066.
(86) Zhang, Y.; Ma, N.; Wang, T.; Fan, J. Work function Regulation of Surface-engineered Ti_2CT_2 MXenes for Efficient Electrochemical Nitrogen Reduction Reaction. *Nanoscale* **2022**, *14*, 12610−12619.
(87) Guo, Y.; Wang, T.; Yang, Q.; Li, X.; Li, H.; Wang, Y.; Jiao, T.; Huang, Z.; Dong, B.; Zhang, W.; Fan, J.; Zhi, C. Highly Efficient Electrochemical Reduction of Nitrogen to Ammonia on Surface Termination Modified $Ti_3C_2T_x$ MXene Nanosheets. *ACS Nano* **2020**, *14*, 9089−9097.

https://doi.org/10.1021/acsomega.5c04416
ACS Omega 2025, 10, 32310−32325